3DVAR and Cloud Analysis with WSR-88D Level-II Data for the Prediction of the Fort Worth Tornadic Thunderstorms Part II: Impact of Radial Velocity Analysis via 3DVAR

Ming Hu[1,2], Ming Xue[*1,2], Jidong Gao[1] and Keith Brewster[1]

[1]Center for Analysis and Prediction of Storms and
[2]School of Meteorology
University of Oklahoma, Norman, OK 73019

[*]Corresponding Author Address:
Ming Xue
School of Meteorology, University of Oklahoma,
100 East Boyd, Norman, OK 73019
E-mail: mxue@ou.edu.

ABSTRACT

In this two-part paper, the impact of Level-II WSR-88D radar reflectivity and radial velocity data on the prediction of a cluster of tornadic thunderstorms in the Advanced Regional Prediction System (ARPS) model is studied. Radar reflectivity data are used primarily in a cloud analysis procedure that retrieves the amount of hydrometeors and adjusts in-cloud temperature, moisture and cloud fields, while radial velocity data are analyzed through a three-dimensional variational (3DVAR) scheme that contains a 3D mass divergence constraint in the cost function. In Part I, we discussed the impact of the cloud analysis and modifications to the scheme. In this part, we study the impact of radial velocity data and the mass divergence constraint in the 3DVAR cost function.

The case studied is that of the 28 March, 2000 Fort Worth tornadoes. The addition of the radial velocity improves the forecasts beyond that experienced with the cloud analysis alone. The prediction is able to forecast the morphology of individual storm cells on the 3-km grid up to two hours; the rotating supercell characteristics of the storm that spawned two tornadoes are well captured; timing errors in the forecast are less than 15 minutes and location errors are less than 10 km at the time of the tornadoes.

When forecasts were made with radial velocity only, they failed to predict nearly all storm cells. Using the current 3DVAR and cloud analysis procedures with 10-minute intermittent assimilation cycles, reflectivity data are found to have a greater positive impact than radial velocity. The use of radial velocity does improve the storm forecast when combined with reflectivity assimilation, by, for example, improving the forecasts of the strong low-level vorticity centers associated with the tornadoes. Positive effects of including a mass divergence constraint in the 3DVAR cost function are also documented.

1. Introduction

This is the second part of a two-part study investigating the impact of radar data on the prediction of a cluster of tornadic thunderstorms. In Hu et al. (2005, hereafter Part I), the conventional data are analyzed via a three dimensional variational (3DVAR) analysis system, while reflectivity data are used through a cloud analysis procedure to define hydrometeor and cloud fields and to make adjustments to in-cloud temperature and moisture fields.

The 3DVAR analysis system used in this study is developed within the ARPS model (Xue *et al.* 1995; Xue *et al.* 2000; Xue *et al.* 2001) framework and documented in Xue et al (2003) and Gao et al (2002; 2004)**.** The cloud analysis procedure has evolved from that used in the Local Analysis and Prediction System (LAPS, Albers *et al.* 1996) with previous enhancements documented in Zhang et al (1998) and Zhang (1999). This cloud analysis is a component of both the ARPS 3DVAR and ADAS (ARPS Data Analysis System, Brewster 1996) systems. In the experiments by Xue et al. (2003, hereafter Xue03), the ADAS and an early version of ARPS cloud analysis were used with WSR-88D Level-III (NIDS) data to provide initial conditions for the ARPS to predict the Fort Worth, Texas, tornadic thunderstorm case of 28 March, 2000. Since then, several improvements have been made to the cloud analysis procedure.

Using the ARPS 3DVAR instead of the ADAS as the analysis tool, the Level-II instead of Level-III radar data, together with an improved version of the ARPS cloud analysis and an updated version of the ARPS model, experiments in Part I studied the impact of the improvements in the cloud analysis procedure and of each modification individually on the same Fort Worth case.

It is found that the detailed storm information in the initial temperature and hydrometeor

fields added by the cloud analysis using radar reflectivity data is critical for successful storm forecast. The experiment with a complete set of recent modifications to the cloud analysis improves the prediction of the main tornadic thunderstorm. Part I also documented the impact by each individual modification in the cloud analysis scheme on the assimilated state and the evolution of the storms in the forecast. In this second part (Part II), we examine the impact of radial velocity data through a series of assimilation experiments. The organization of this paper is as follows. In section 2, we briefly introduce the ARPS 3DVAR system, including the important aspects of radial velocity analysis and the mass divergence constraint. In section 3, we describe the tornado outbreak case briefly and the design of experiments. Detailed results are presented in section 4 and a summary is provided in section 5.

2. The ARPS 3DVAR system

a. The basic scheme

Following Gao et al. (2004), the standard cost function of 3DVAR can be written as

$$J(\mathbf{x}) = \frac{1}{2}(\mathbf{x}-\mathbf{x}^b)^T \mathbf{B}^{-1}(\mathbf{x}-\mathbf{x}^b) + \frac{1}{2}\left[H(\mathbf{x})-\mathbf{y}^o\right]^T \mathbf{R}^{-1}\left[H(\mathbf{x})-\mathbf{y}^o\right] + J_c(\mathbf{x}), \qquad (1)$$

where the first term on the right hand side measures the departure of the analysis vector, *x,* from the background, x^b, weighted by the inverse of the background error covariance matrix **B**. In the current ARPS 3DVAR system, the analysis vector *x* contains the three wind components (*u, v,* and *w*), potential temperature (θ), pressure (*p*) and water vapor mixing ratio (q_v). The second, observation term, measures the departure of the analysis from the observation vector, $\mathbf{y}^o$. The analysis is projected to the observation space by the forward operator, *H,* and the observation term is weighted by the inverse of observation error covariance matrix **R** that includes the both instrument and representativeness errors. The forward operator errors, especially those for

conventional data, should be small and are usually neglected. Term $J_c(\mathbf{x})$ in Eq. (1) represents dynamic or equation constraints.

Transforming control variables from $\mathbf{x}$ to $\mathbf{v}$, according to $\mathbf{B}^{1/2}\mathbf{v} = (\mathbf{x} - \mathbf{x}^b)$, the standard cost function is changed into incremental form for new control variable $\mathbf{v}$:

$$J_{inc}(\mathbf{v}) = \frac{1}{2}\mathbf{v}^T\mathbf{v} + \frac{1}{2}\left(\mathbf{HB}^{1/2}\mathbf{v} - \mathbf{d}\right)^T \mathbf{R}^{-1}\left(\mathbf{HB}^{1/2}\mathbf{v} - \mathbf{d}\right) + J_c(\mathbf{v}), \tag{2}$$

where $\mathbf{H}$ is the linearized version of H and $\mathbf{d} \equiv \mathbf{y}^o - H(\mathbf{x}^b)$. In the current system, the cross-correlations between variables are not included in the background error covariances. The spatial covariances for background error are modeled by a recursive filter. Following common practice, observation errors are assumed to be uncorrelated, hence the corresponding covariance matrix, $\mathbf{R}$, is diagonal, and its diagonal elements are specified according to the estimated observation errors. Correlated observation errors are usually removed through bias correction procedures before or within the analysis procedure (e.g., Harris and Kelly 2001).

Considering that we are dealing with flows at vastly different scales and different data types also represent very different spatial scales, the ARPS 3DVAR allows for the use of multiple analysis passes, with each one including different data types and using different filter scales. The selection of the filter scales are guided by the density of observational data to which filter is applied. We call this a multi-scale analysis procedure.

b. Radar radial velocity data

For the radial velocity observations, the forward operator, or H in Eq.(1), that projects the velocity into the radial direction, is

$$V_r = \frac{(x - x_0)u + (y - y_0)u + (z - z_0)w}{r}, \tag{3}$$

4

where u, v and w are the wind components in Cartesian coordinates (x, y, z); and (x_0, y_0, z_0) are the coordinates of radar; r is the distance from the radar location to the observation points of radial velocity. In the ARPS 3DVAR, the observed radial velocity data are first interpolated to analysis grid points through preprocessing and therefore no further spatial interpolation is needed in this forward operator. The actual preprocessing program also includes quality control (velocity dealiasing, clutter removal, etc.) and takes into account the spherical geometry of the earth and the curved path of the radar beam.

c. Mass divergence constraint

In the ARPS 3DVAR, the following weak mass divergence constraint is imposed on the analyzed wind field:

$$J_c = \frac{1}{2}\lambda_c^2 D^2, \tag{4}$$

where λ_c is a weighting coefficient that controls the relative importance of this penalty term in the cost function. D has the form of

$$D = \alpha\left(\frac{\partial \bar{\rho} u}{\partial x} + \frac{\partial \bar{\rho} v}{\partial y}\right) + \beta \frac{\partial \bar{\rho} w}{\partial z}, \tag{5}$$

where $\bar{\rho}$ is the mean air density at given height levels, α and β are weighting coefficients for the horizontal and vertical terms, respectively. Different choices of the α and β values will be tested in a set of analysis experiments to be presented later. This constraint acts to couple the wind components together during the analysis. When $\alpha = \beta = 1$, the constraint acts to minimize the three-dimensional mass divergence and weakly enforces anelastic mass continuity. Gao et al (1999; 2004) found, for their case of near-unity grid aspect ratio ($\Delta x \sim \Delta z$), that the 3D formulation is effective in producing reasonable analyses of vertical as well as the horizontal

velocity in their dual-Doppler wind analyses.

When used in a finite difference form, we found that the vertical mass divergence term in Eq. (5) dominates the adjustment of J_c in cases where the vertical grid is stretched to a large Δx to Δz (grid aspect) ratio at the low levels. For example, when $\Delta x = \Delta y = \gamma \Delta z$, Eq. (5) is discretized as

$$D = \frac{\Delta(\bar{\rho}u) + \Delta(\bar{\rho}v)}{\gamma \Delta z} + \frac{\Delta(\bar{\rho}w)}{\Delta z} \ . \tag{6}$$

When the grid aspect ratio, γ, is large, say over 100, as in our case near the surface, a small adjustment in the vertical velocity can offset a large change in the horizontal wind divergence. The result is that little change due to this constraint is made by the minimization to the horizontal wind components. One possible solution, as used here, is to use different values of α and β or even set β to zero to alleviate this artifact of discretization.

To illustrate the above points, we conducted three experiments, in which a single radial velocity observation (taken to be along the x direction) is analyzed, using (a) no mass divergence constraint ($\alpha = \beta = 0$), (b) using a 2D mass constraint ($\alpha = 1$, $\beta = 0$), and (c) using a fully 3D mass divergence constraint ($\alpha = \beta = 1$). Further, to isolate the effect of the constraint, we do not include spatial filtering in these tests. The results of these experiments are plotted in Fig. 1. It can be seen that without the constraint, no y component (or cross-beam component) of velocity is produced by the analysis, i.e., the analysis is purely uni-variant (Fig. 1a). In this case no vertical velocity is created either (not shown). When the 2D mass divergence is used, a single radial velocity observation induces a horizontal flow pattern that is nearly non-divergent (Fig. 1b) while no vertical velocity develops (not shown). When a complete 3D divergence appears in J_c, most of the wind adjustment due to the constraint occurs in vertical velocity, as is shown by Fig.

1c, while little adjustment occurs to the *y* (horizontal cross-beam) component (Fig. 1d), a result very similar to the unconstrained case. In addition, when the spatial filtering (via recursive filter) is applied, the analysis appears smoother and the analysis increment spreads over a larger area but the general behavior remains the same (not shown).

The main goal of including mass divergence constraint in the radial velocity analysis is to deduce wind information perpendicular to radar beams. From the above analysis, the three-dimensional mass divergence constraint cannot achieve the desired effect in the horizontal flow when the grid aspect ratio is large, which is unfortunately true in our case. This was not an issue in our earlier variational dual-Doppler wind analyses (Gao et al. 1999; 2004) and has therefore not been recognized until now. For the above reason, the weak two-dimensional mass divergence constraint is used in the control and related experiments and an additional set of experiments is performed to examine the impact of different formulations of the constraint on the analysis and forecast. Since it is a weak constraint, zero mass divergence is not strictly satisfied, the analysis has some flexibility in determining the amount of adjustment to different wind components, depending on the weighting coefficients.

3. Fort Worth tornado case and design of forecast experiments with ARPS

The same tornadic thunderstorm outbreak case studied in Part I is used here to examine the impact of radial velocity data and mass divergence constraint. This case consists of an F2 (maximum winds 51 m s^{-1} to 70 m s^{-1}) tornado which struck downtown Fort Worth, Texas (TX), at around 6:15 pm LST 28 March (0015 UTC 29 March), 2000. The tornado vortex developed directly over the city, descended, and stayed on the ground for at least 15 minutes. A second tornado from the same cell touched down in south Arlington, approximately 25 kilometers east of Fort Worth, about 45 minutes later, at around 7:00 pm LST 28 March (0100 UTC 29 March),

2000.

Using the same configuration as Part I, assimilation and prediction experiments are conducted. These experiments use two one-way nested grids with horizontal grid spacing of 9 and 3 km. The two grids cover areas of 1000 ×1000 and 450×300 km^2, respectively. Full model physics are employed in the forecasts of both grids except for cumulus parameterization. On the 9-km grid, a 12-hour model forecast is started from a single 3DVAR analysis at 1800 UTC 28 March and uses the National Center for Environmental Prediction (NCEP) Eta 1800 UTC forecasts at 3-hour intervals as lateral boundary conditions.

On the 3-km grid, both WSR-88D full-volume (Level-II) reflectivity and radial velocity data are analyzed in 10-minute intermittent assimilation cycles that begin at 2200 UTC and continue for one hour. The forecast, with the same model settings as Part I, was started from the assimilated initial condition at 2300 UTC and ended at 0200 UTC 29 March.

Three analysis passes are performed on the 3-km grid, with each pass using different data types. For the wind profiler data used in the first pass, a 120-km filter scale is used. Filter scales of 75 and 9 km are used in the second and third passes when surface data and radial velocity data are used, respectively.

In this paper, results from eight 3-km experiments, including a control, are reported (see Table 1). The first three are designed to specifically investigate the impact of assimilating radar data. The control experiment, CNTLVR, includes both Level II reflectivity and radial velocity data in its assimilation cycles. A two-dimensional version of mass divergence constraint is imposed. Two other experiments, namely CNTLZ and VR, examine the effect of including reflectivity (denoted as Z), or radial velocity (denoted as V_r) data alone. The experiments are otherwise the same as CNTLVR.

The next five experiments are designed to examine the role and effect of various formulations of the mass divergence constraint in the 3DVAR cost function (Table 1). They differ from CNTLVR in the use of the constraint only. Experiment NoDiv does not include any divergence constraint while experiments Div3Da and Div3Db use a 3D formulation with different and equal values of α and β in Eq. (5), respectively. Two other experiments, Div2Da and Div2Db, test the sensitivity of storm forecasts to weighting coefficient, λ_c, with a 2D formulation (Table 1).

4. Results of assimilation and forecast experiments

In this section, we first discuss the forecast of control experiment CNTLVR by comparing the forecast radar reflectivity fields to the observed ones. The forecasts of CNTLZ and VR are then analyzed to examine the additional impact of radial velocity data. The results of assimilation from these three experiments are also inter-compared. Finally, the results from the experiments with different formulations of the mass divergence constraint are discussed.

a. Radar observations and forecasting results of control experiment

Since both tornadoes occurred between 0000 UTC and 0100 UTC 29 March in the Fort Worth area, we focus our discussion of the forecast on this period. For direct comparison with radar observations, we derive reflectivity from model-predicted hydrometeor fields that also take into account of the ice phases, and the reflectivity equations follow mostly Smith et al. (1975), with the actual formulations used given in Tong and Xue (2005). The predicted reflectivity fields from the control run, which included both reflectivity and radial velocity data, are mapped to the 1.45° radar elevation of the KFWS radar (labeled in the plots) and plotted in the right column of Fig. 2 at 15 minute intervals for a 1 hour period starting from 0000 UTC 29 March. The corresponding observed reflectivity fields are plotted in the left column. Fort Worth and

9

Arlington are labeled in Fig. 2b.

At 0000 UTC 29 March, five individual thunderstorms can be identified near Forth Worth from the radar observations (Fig. 2a). They are labeled A, B, C, C' and D in the plots. Storm A is the storm that spawned the downtown Fort Worth tornado at around 0015 UTC and the Arlington tornado 45 minutes later. Storm B approached Storm A from the west, during the period 0000 UTC to 0045 UTC (Fig. 2a, c, e, g) and then merged with Storm A to form a combined storm that we re-label as F (Fig. 2i) at 0100 UTC. Storms C and C' formed near the end of the assimilation window, propagated towards Storm A from the south and also merged with Storm A (Fig. 2, left column) by 0100 UTC. Storm D was initially located near the northeast corner of Hill County (see Fig. 2a for county locations) and later propagated northeast into Ellis County. Storm D was initiated during the assimilation window and remained strong throughout the period of tornadoes. The complex interactions among these storm cells pose a major challenge for accurate forecasting of the morphology of these storms.

The one-hour model forecast at 0000 UTC 29 March, also depicts five storm cells in the vicinity of Fort Worth (Fig. 2b). Four of them can be directly linked to an observed one (Fig. 2a), but the one labeled C" has no real world counterpart. Storms A and B have location errors of about 20-25 km while Storms C and D have position errors of less than 5 km. Observed Storm C' is missed by the forecast at its location near the southwest corner of Tarrant County while the model placed a storm cell, C", further to the south, in west-central Johnson County. When we examine the forecast during the first hour (2300-0000 UTC, not shown here), it is found that all storm cells that existed at the beginning of forecast underwent varying degrees of adjustment. Storms A and B weaken initially and grow again from 2345 UTC, while Storm C remains relatively weak until about 2350 UTC. Given that little information on Storm C was provided by

the radar or the assimilation process, the model did a good job in initiating Storm C. Apart from some error in propagation speed (a little too fast), Storm D is well predicted throughout the period by the model. Both the observed and predicted low-level reflectivity of Storm D show clear hook echo shapes.

Fig. 3 shows the predicted wind vector and vertical vorticity fields from the control experiment at the surface (left column) and 3 km MSL (approximately 2.8 km AGL, right column) at the same times as the reflectivity fields shown in Fig. 2. From the surface wind field at 0000 UTC, strong and fairly isolated convergence centers are indicated for Storms A, B and D (Fig. 3a). The gust fronts associated with the downdrafts of storms A and B are still relatively weak at this time while a much stronger downdraft is found to the northwest of A, associated with a storm that is decaying. Vertical vorticity associated with A is still weak at the surface. In the flow field at 3 km MSL, however, a strong vorticity maximum is found within Storm A (Fig. 3b).

Fifteen minutes later, at 0015 UTC, the time of the formation of the Fort Worth tornado, both predicted Storms A and B are enhanced significantly (Fig. 2d). The location error of the maximum reflectivity center of Storm A is reduced significantly, to within 10 km of the observed one (Fig. 2c, d). The predicted locations of B and C are also very accurate at this time. Spurious Storm C" remains and appears as a strong reflectivity center. Storm D moved east a little too fast in the 15-minute period, with the reflectivity core entering Ellis County by this time. The wind fields exhibit a strong convergence center and a weak vorticity center at the surface (Fig. 3c) but a strong vorticity center at 3 km MSL (Fig. 3d) associated with A. The convergence and vorticity centers related to Storm B are also enhanced. A new spurious storm south of Storm B is generated by collision of gust fronts from Storms B and C (Fig. 2d and Fig. 3c). These results

11

show that the main Storm A is predicted with high low-level reflectivity and strong mid-level rotation and approaches Fort Worth city from the northwest. Despite some delay in the intensification of low-level rotation in the forecast, it contains clear indications of the potential of a tornado from this cell.

In reality, an F2 tornado spawned from Storm A struck downtown Fort Worth from 0015 UTC to 0030 UTC. At 0030 UTC, the control forecast gives good indications, in both reflectivity and wind fields, of possible tornadogenesis from Storm A. The predicted reflectivity matches very well with observation (Fig. 2e, f). The southern flank of the predicted storm is sweeping through Fort Worth city consistent with the observations at this time. The weaker surface vorticity center found in Fig. 3c earlier has developed into a strong vorticity center by 0030 UTC, with a maximum value of about $1.5 \times 10^{-3} s^{-1}$ (note that the grid resolution is 3 km, which is very coarse for the estimation of vorticity associated with tornadoes), and the maximum is located almost right over Fort Worth (Fig. 3e). Colocated with the vorticity maximum is also strong surface convergence, indicating the presence of strong near-surface updraft and associated vertical stretching. An isolated maximum vorticity center within Storm A is even better defined at 3 km MSL (Fig. 3f) but is not as strong as it was at 0015 UTC. The intensification of ground level vorticity and slight weakening of mid-level rotation suggest shifting of strong rotation to the lower levels, which typically occurs during tornadogenesis and in the later life cycle of tornadoes (see, e.g., Davies-Jones 2001). The development of this strong, well-organized, deep vorticity column during the period that coincides with the Fort Worth tornado indicates good fidelity of the predicted storm, even though the model resolution is much too coarse to produce flow on the scale of a tornado or even the tornado's parent vortex. Simulations starting from the analyzed initial conditions but at much higher resolutions are planned.

At 0030 UTC, Storm B is also reproduced well by the forecast as seen from the reflectivity field. The spurious storm cell to its south found at 0015 UTC has merged with Storm B by this time. The vorticity center related Storm B is much weaker than that of Storm A at both the surface and 3 km MSL. Predicted Storm C covers the area of observed Storms C and C' and there is no identifiable surface vorticity center associated with it. Predicted Storm D is located northeast of the observed one by about 10 km because of its faster northeastward propagation. At this time, the main characteristics of the storm cells A through D are all very accurately predicted by the model, and the representations are an improvement over that reported in Xue03 as well as that of control experiment of Part I, which did not include radial velocity data.

At around 0045 UTC, the reflectivity core of Storm A has moved to eastern Tarrant County, near Arlington, and a well-organized, deep and stronger vorticity column is nearly colocated with Arlington (Fig. 2g, h and Fig. 3g, h), which indicates high potential of tornadogenesis at this area. The surface maximum vorticity is now 2.4×10^{-3} s^{-1}, even higher than earlier. The model successfully predicts Storm B's decay and merger with Storm A around this time. The predicted Storm C lags behind the observed one by nearly 30 km and does not merge with Storm A as the real one did. The forecast for Storm D matches the observed radar echoes well. At the surface, the northwest side of outflow of Storm D is approaching Storm A located to its northwest, which probably contributed to the weakening of Storm A and its subsequently merged storm.

In reality, Storms A, B and C merged together and formed Storm F that produced the Arlington tornado at 0100 UTC 29 March (Fig. 2i). The model has some success at forecasting this process, as the predicted Storms A and B did merge and Storm C's reflectivity field became combined with A and B's although its core remain separate at 0100 UTC. Further, the predicted

reflectivity maximum center has a displacement to the northeast (Fig. 2j). Predicted Storm D remains strong, as the observed one, and again is located slightly ahead of the observed storm. At the surface, maximum vorticity centers associated with the Storms A and D are still clearly identifiable (Fig. 3i), but the one associated with the Storm A is weaker with the former. At 3 km MSL, the disturbances and vorticity that appear to be associated with the decaying Storm C may be too strong (Fig. 3j); we do not have good data to verify their fidelity, however.

Based on the results of our control experiment, it can be concluded that starting from an initial condition that assimilates WRS-88D radar Level II data together conventional observations through the 3DVAR and cloud analysis, the model is able to predict the timing, location and key characteristics of convective storms with good accuracy. The accurate prediction of the development of a strong, well-organized, deep vorticity column associated with the tornadic storm in a period spanning the two observed tornado outbreaks is especially encouraging. Our results also show that when several storms are spaced closely, complex storm interactions can occur, through, for example, gust front collisions. Spurious cells can be triggered when such interactions are incorrectly or inaccurately handled by the model. Such a situation requires an accurate analysis of all aspects of the convective storms.

b. Forecasting results of experiment using reflectivity only

In this subsection, the forecasting results from experiment CNTLZ, which has been discussed in Part I, are compared to those of CNTLVR. The two experiments differ only in that CNTLZ does not include radial velocity data.

The predicted reflectivity fields from experiment CNTLZ, as shown before, are plotted in Fig. 4 at 15 minute intervals for a half hour starting from 0015 UTC 29 March. The predicted wind and vorticity fields at the corresponding times are given in Fig. 5 for the surface (left

column) and 3 km MSL (right column).

During the period shown, CNTLZ also reproduced the main characteristics of Storm A quite successfully (compare Fig. 2c, e, g and Fig. 4) although the location errors are somewhat larger than that of CNTLVR from 0030 to 0045 UTC (compare Fig. 2d, f, h and Fig. 4). Both experiments also give similar forecast for Storm D and spurious Storm C". Predicted Storm B in experiment CNTLZ appears as a large area of weak reflectivity at 0015 UTC and disappears after that time. Instead of merging with Storm B, Storm A is followed by and merges with a strong spurious Storm A', which is triggered by a collision of the gust fronts from Storms A, B and C" at 0015 UTC (Fig. 5a). The forecast of CNTLZ also misses observed Storm C in this period. Overall, the forecast of CNTLZ is not as good as that of CNTLVR and the differences clearly demonstrate the positive impact of assimilating additional radial velocity data in CNTLVR.

This positive impact can be seen more clearly in the wind and vorticity field. The well-organized, deep column of strong vorticity that develops near Fort Worth and moves to Arlington during this half hour in the forecast of CNTLVR does not exist in the forecast of CNTLZ (Fig. 3 and Fig. 5). CNTLZ does not develop a strong surface vorticity center within Tarrant County, and the 3 km MSL vorticity maxima found at 0015 and 0030 UTC have larger displacement errors. By 0045 UTC the 3 km MSL vorticity maximum is considerably weaker than the one depicted in the control experiment. The differences in morphology of these features indicate that the forecast of the wind fields has been improved significantly by assimilating radial velocity data via our 3DVAR analysis.

The equitable threat scores (ETS, Schaefer 1990) of predicted reflectivity at the 1.45º elevation for the 5, 15, 30 and 45 dBZ thresholds are plotted in Fig. 6. From the figure, we can

see a tendency for the scores to decrease quickly in first hour of forecast then increase in second hour for all four thresholds. This U-shape of ETS curves for all cases is due to the imbalance among different variables, especially for wind and temperature, in the initial analysis. During the initial period of forecast, significant adjustments occur in the model among the cloud variables for them to better fit the model dynamics and physics. Also, during the period, the reflectivity is over-predicted and some spurious cells are created. Thus, the ETS decreases during this adjustment period. After the initial adjustment, the main characteristics of observed cells are better captured in the forecast and the ETS score increases. The reason of the lowest score at 0000 UTC is complex. It is related the limitations of both analysis procedure (the ability of generating balanced initial fields) and model (the ability to establish a suitable balance quickly).

It can be seen that all scores in the 45 dBZ threshold are better for CNTLVR than for CNTLZ from a little after 0000 UTC to 0100 UTC (Fig. 6d), in agreement with the earlier subjective assessment of the forecast of cell centers. The improvement of CNTLVR over CNTLZ for other thresholds are not as evident during this hour, although the score is generally better at 0100 UTC, while the score is lower at 0045 UTC for the other three thresholds (The scores for experiment NoDiv will be discussed later). Our subjective analysis does suggest that the forecast of CNTLVR is superior at 0045 UTC, however, and the high threshold (45 dBZ) ETS confirms this. The less than clear cut signal from the ETS suggests that the ETS should be used carefully for evaluating forecasts containing discrete features, for which propagation and mis-positioning errors can have a significant impact on the calculated scores.

c. Forecasting results of experiment using radial velocity only

In the previous subsection, we found that radial velocity data, when used (via the 3DVAR analysis) together with reflectivity data (via the cloud analysis), can positively impact a storm

forecast. In this subsection, we present results from experiment VR in which the cloud analysis with reflectivity data was not performed, while radial velocity is assimilated the same way as in control experiment CNTLVR.

The predicted reflectivity field from experiment VR mapped to the elevation 1.45° is plotted in Fig. 7 at 0030 UTC 29 March, which is in-between the times of the two tornadoes.

Compared to the observed reflectivity (Fig. 2e), it can be seen that experiment VR completely failed to predict storm cells around Fort Worth (Fig. 7). There are two storm cells to the southwest of Tarrant County and they originated from the 9-km forecast that was used as the background for the initial 3-km analysis at 2200 UTC. The storms do not match the observed reflectivity, indicating a failure of forecast to build and support storm cells in a short-term forecast. Still, some positive impact of assimilating radial velocity data can be found during and shortly after the assimilation cycles. The fields of VR show weak reflectivity centers to the northwest of Fort Worth at the end of assimilation cycles. They decay, however, soon after the forecast period begins (not shown).

The above results tell us that assimilating the radial velocity alone via the current 3DVAR procedure is far from enough to create a properly balanced storm in this case. This is not very surprising because the availability of radial velocity data from a single radar, and the lack of strong, reliable link between radial velocity data with other model variables, particularly the buoyancy. More sophisticated equation constraints that better couple model state variables together or flow-dependent background error covariances should help. The former is true with 4DVAR and the latter with the ensemble Kalman filter method. Tong and Xue (2005) found with observing system simulation experiments (OSSE) that radial velocity has a greater positive impact than reflectivity when assimilated using ensemble Kalman filter method for a simulated

17

supercell storm. Radial velocity also plays a key role in 4DVAR assimilation work as discussed by Sun and Crook (1997).

Based on the above results, we conclude that the assimilation of both radial velocity and reflectivity data from a single Doppler radar via an inexpensive intermittent assimilation procedure that involves the 3DVAR and cloud analyses is effective to build pre-existing storms in a nonhydrostatic model at a marginally storm-resolving 3-km resolution. The forecast starting from the assimilated initial condition is able to capture most of the key characteristics of the observed storms for a two-hour period. Although reflectivity data are found to have a greater positive impact on the storm forecast than radial velocity with the current analysis procedure, the use of radial velocity along with reflectivity do improve the quality of forecast. The impact of the radial velocity assimilation was most evident in the strong low-level vorticity centers associated with the expected tornadogenesis.

The possible reason for the smaller impact of radial velocity data is that the initial thermal, moisture and cloud field disturbances introduced by the reflectivity can sustain during forecast and induce corresponding changes in wind field but initial wind disturbances from radial velocity disperse quickly in the form of acoustic waves in the absence of proper balances with other fields and among the three wind components themselves.

d. Comparison of assimilation results

To understand the above forecast results further, the impact of assimilating radar observation on the assimilated initial conditions are examined here. The vertical velocity, w, fields at 5 km MSL from the assimilation output of experiments CNTLVR, CNTLZ and VR are plotted in the left column of Fig. 8, while the corresponding cross section of w along a line through storms A and B are plotted in the right column of the same figure.

18

At the end of the assimilation period, the strong, isolated updraft centers related to Storms A and B are well established in both experiments CNTLVR and CNTLZ (Fig. 8a, b, c, and d). When only radial velocity data are analyzed (experiment VR), the updrafts are much weaker (Fig. 8e and f). Starting form these initial conditions, the forecasts of CNTLVR and CNTLZ are expected to be better. Still, for experiment VR, the updrafts are colocated with the observed cells, indicating that the 3DVAR analysis of radial velocity does add useful storm information into the initial fields.

Comparing CNTLVR and CNTLZ (Fig. 8a, b, c and d), the updrafts of CNTLZ are much stronger than those of CNTLVR. This indicates that the 3DVAR analysis of radial velocity data acts to constraint the magnitude of updraft. In CNTLVR, the updrafts of storms A and B are dominant and show some hook shape on their southern flank, while in CNTLZ much stronger updrafts exist, with the strongest one being associated with a storm north of storm A. The radar observations indicate that storms A and B are at their early stage of development while the cells north of them are in a decaying stage. This suggests that the analysis of radial velocity data correctly improves the relative strength and structure of the cells in the initial condition and contributes to the improvement of forecast.

Next, we will examine various formulations of the mass divergence constraint.

e. Experiments on mass divergence constraint

All of the above experiments that assimilate radial velocity data use a two-dimensional mass divergence as a weak constraint. To better understand the impact of the divergence constraint, five additional experiments, namely, NoDiv, Div2Da, Div2Db, Div3Da, and Div3Db, are conducted. For brevity, we mainly present the results of these experiments at 0030 UTC 29 March, corresponding to 1.5 hour forecast time. The predicted reflectivity mapped to the same

19

1.45° radar elevation of KFWS radar is plotted in Fig. 9 for CNTLVR and the above five experiments. The corresponding surface and 3 km MSL wind and vorticity fields are plotted in Fig. 10. The ETS scores for reflectivity for these experiments are plotted in Fig. 11 and Fig. 12, together with those for CNTLVR. The ETS scores for NoDiv are also plotted in Fig. 6 instead for easier comparison with those of CNTLVR and CNTLZ.

1) Importance of divergence constraint

Experiment NoDiv in which mass divergence constraint is not imposed at all is designed to separate the effect of mass divergence from that of radial velocity data. Comparing Fig. 9b with the corresponding observation in Fig. 2e, it is seen that Storm A is over-predicted by NoDiv in size and its location has a southward displacement while Storm B is completely missed. Storm D is located too far to the east, by approximately 30 km, and it is trailed by a spurious, though weaker, cell to its west. Another spurious cell, labeled D' in the figure, is found to the north-northeast of cell D. It is labeled D' because it is a cell that split from Storm D in the first half hour of forecast (not shown). As shown in Fig. 9a for this time and discussed in detail for other times earlier, the forecast of CNTLVR is clearly more accurate than that of NoDiv. The ETS of NoDiv for the 45dBZ threshold are lower than both CNTLVR and CNTLZ during the important period between 0000 and 0100 UTC (Fig. 6d).

The above comparisons demonstrate the importance of including mass divergence constraint when analyzing radial velocity data. This is because, as discussed earlier, a single Doppler radar observes wind along the radial direction only. The cross-beam components cannot be determined by the 3DVAR analysis without additional information that links the three components. Without any constraint, 3DVAR tends to make adjustments of background winds along the radial direction only, leaving the other components essentially unchanged. The

inclusion of a mass divergence constraint forces the other wind components to respond to changes along the radial direction. Further, large amplitude acoustic oscillations are found in the time series plots of surface pressure in NoDiv (not shown). Imposing the mass divergence constraint helps control such noise. Treating the constraint as a weak constraint gives the system necessary flexibility, as discussed for dual-Doppler analysis by Gao et al (1999). In the case of dual-Doppler wind analysis, two of the three wind components can be determined while the mass-continuity equation gives the third, yielding an easier problem than we have here.

2) Sensitivity to weighting coefficient of divergence constraint

The sensitivity of storm forecast on weighting coefficient, λ_c, of the mass divergence constraint in the cost function is studied through experiments Div2Da and Div2Db in which λ_c is half or double the value of CNTLVR (Table 1), respectively. In the 1.5-hour forecasts of these three experiments (Fig. 9a, c, d), the storms show a similar general pattern with several differences in the fine structures. First, Storms A and B in experiment Div2Db are not separate as in the other two experiments and in the real world. Second, the maximum reflectivity center of Storm A in Div2Db has greater displacement errors. Third, Storm D in Div2Da and Div2Db has a greater eastward displacement error than in CNTLVR. Although the pattern comparison shows that the forecast of experiment CNTLVR is somewhat better than that of Div2Da and Div2Db at this time, the latter achieved generally better ETS (Fig. 11). For the 45 dBZ threshold, Div2Db outperforms the other two at 0030 UTC, but overall, the scores of the three are similar. In general, it appears that the analysis and forecast are not very sensitive to the coefficient of the divergence constraint for this case.

3) Effects of divergence constraint formulations

In section 2c, we illustrated the problem with using a 3D mass divergence constraint on a grid with large aspect ratios. In such a situation, the vertical part of the mass divergence dominates the wind adjustment so that horizontal wind components are little adjusted. This is the main reason why a 2D mass divergence constraint is used in all the earlier experiments. It should be pointed out, however, the 2D mass-divergence constraint is not really physical for convective scale flows, which can exhibit significant horizontal divergence beneath strong updrafts. To study this problem further, two experiments employing 3D mass divergence constraint are performed. Experiment Div3Da uses different weighting coefficients for the horizontal and vertical parts of the 3D mass divergence constraint while experiment Div3Db uses the same weighting coefficient for both parts, which is effectively a true 3D mass divergence constraint. The exact values of the weighting coefficients are listed in Table 1.

As we expected, experiment Div3Db gives very similar forecast for main storm cells at 0030 UTC as experiment NoDiv (Fig. 9b, f) because almost all wind adjustment were applied to the vertical velocity, and the adjustment is expected to be one order of magnitude smaller (because of large aspect ratio) than those of the horizontal winds for the 3D mass divergence constraint to be satisfied. The ETS of Div3Db and NoDiv shown in Fig. 12 are also similar for most of the times and threshold values, consistent with our subjective evaluation.

Experiment Div3Da decreases the weighting coefficient for the vertical divergence by a factor of ten compared to CNTLVR or the horizontal term in Div3Da. Doing so decreases the effect of vertical velocity adjustment thereby giving greater adjustments to the horizontal winds. The forecast reflectivity field plotted for Div3Da in Fig. 9 looks similar to that of Div2Db, and is better than that of Div3Db, indicating the increased role of adjustments to horizontal wind fields.

The ETS of experiment Div3Da for the 45dBZ threshold are in-between those of experiments CNTLVR and NoDiv (Fig. 12d).

The surface and 3 km MSL wind and vorticity fields from the above five experiments, (i.e., NoDiv, Div2Da, Div2Db, Div3Da, and Div3Db) are plotted in Fig. 10 and they can be compared to the corresponding times of CNTLVR in Fig. 3. Interestingly, all five experiments predicted a well-defined, column of high vorticity over Fort Worth just as in experiment CNTLVR, but their shape and intensity differ somewhat. However, considering the fact that the forecast with no radial winds (experiment CNTLZ) failed to produce this high vorticity column, we can credit the radial velocity for the formation of this mesocyclone.

4) Results of assimilation from divergence constraint experiments

The vertical velocity, w, fields at 5 km MSL from the assimilation output of experiments CNTLVR, NoDiv, Div2Da, Div2Db, Div3Da, and Div3Db are plotted in Fig. 13. Although the strengths of updrafts vary significantly among the different experiments, the updrafts of storms A and B are dominant when compared to other updraft centers in the same experiment. Also, the updraft of Storm A shows two centers at this time in most of experiments, which reflects the splitting process of Storm A in this stage just as observed. These features indicate that the analysis of radial velocity data can add useful information to the intrastorm wind fields and explain why the six experiments including radial velocity data produce a stronger low-level vorticity center near the location and time of the Fort Worth tornado.

From Fig. 13, the effects of the mass divergence constraint in reducing the horizontal divergence and updraft intensity can also be clearly seen. Different from the forecast, the strength of the initial updraft is significantly affected by the weighting coefficients in the mass divergence constraint (Fig. 13a, b, c, and d). Again, the similarity between the updrafts of NoDiv

23

and Div3D indicates the problem of applying a 3D constraint on a grid with large grid aspect ratios (Fig. 13b and f).

In summary, we found in this section that the proper implementation of a mass divergence constraint in the 3DVAR analysis increases the positive impact of radial velocity data on the thunderstorm analysis and forecast. But in terms of the predicted wind fields, the differences due to different divergence formulations are much less than the impact of adding radial velocity. In our case of large grid aspect ratios, especially at the low levels, a 2D mass divergence constraint or a 3D formulation with a small coefficient for the vertical component is found to work most effectively.

5. Summary and discussion

In this second part, the impact of Level-II WSR-88D radial velocity data on the prediction of a cluster of tornadic thunderstorms is studied. The similar assimilation and forecast system as Part I are applied to the 28 March, 2000 Fort Worth tornado case. Radial velocity data are used in a 3DVAR analysis that contains a mass divergence constraint in the cost function and reflectivity data are assimilated through a complex cloud analysis procedure.

Results from a total of eight 3-km experiments, which examine the use and impact of Level II radial velocity data from the KFWS radar, are discussed. The results demonstrate that the ARPS 3DVAR is capable of successfully analyzing observations from different sources, including those from radiosonde (available at 1800 UTC), surface stations and Doppler radars. Combined with intermittent assimilation cycles, positive impact of radial velocity data is obtained for the forecast of a cluster of thunderstorms.

The best prediction is obtained when both reflectivity and radial velocity data are assimilated. The prediction is able to predict individual storm cells on the 3-km grid up to two

24

hours into the prediction, and the supercell characteristics of the storm that spawned two individual tornadoes are well predicted, with timing errors of less than 15 minutes, and location errors of less than 10 km at the time of the tornadoes.

The comparison of data denial experiments show that reflectivity data has a greater positive impact on the storm forecast than radial velocity using the current 3DVAR and cloud analysis procedure, while the use of radial velocity along with the reflectivity via the cloud analysis does incrementally improve the storm forecast, especially in terms of the strong low-level vorticity centers associated with the tornadogenesis. When radial velocity (in addition to conventional data) is used without reflectivity, the model fails to forecast nearly all storms around Fort Worth. The small impact of using radial velocity alone is related to the limitation of the current 3DVAR wind analysis procedure which does not make use of radar scans at multiple times and uses only a simple mass divergence constraint that does not solve the under-determinedness problem for single-Doppler wind analysis. Specifically, the lack of buoyancy perturbations associated with the ongoing convection influences negatively the forecast. This is overcome by the cloud analysis scheme which is effective in sustaining the model storms.

It is also found that the use of a mass divergence constraint in the 3DVAR analysis can maximize the positive impact of radial velocity data on the storm forecast. This constraint acts to couple three wind components together during the analysis. Without the constraint, the radial velocity data tends to create too many horizontal discontinuities or small regions of horizontal divergence; the mass divergence constraint, though closer to 2D in formulation, helps smoothing out the small scale features while keeping larger-scale divergence little affected. The divergence at larger scales was beneficial to the support of existing convection.

The rather good forecast of the tornadic thunderstorm in the control experiment shows

that a high-resolution model like ARPS together with an adequate system that assimilates WSR-88D Level II data is able to initialize pre-existing thunderstorms and predict them with reasonable accuracy on the cell-by-cell basis for 2 to 3 hours. The 3-km resolution used here is reachable operationally in the near future, over large enough domains. The need to assimilate radar data every or every other radar volume scans (as done in this study) may place a significant burden on operational systems. For our future studies, we will investigate the impact of assimilation frequency on the analysis and forecast. We also point out the 3DVAR-based procedure used in this study is no more expensive than the ADAS-based procedure used in Xue03.

Our conclusions are, however, based on only one case. Assimilation and forecast experiments with more cases and over extended periods will be valuable in arriving at statistically more reliable conclusions. Such studies are planned. Still, we believe our case study reported here represents an important step towards the eventual goal of effective operational implementation.

References

Albers, S. C., J. A. McGinley, D. A. Birkenheuer, and J. R. Smart, 1996: The local analysis and prediction system (LAPS): Analysis of clouds, precipitation and temperature. *Wea. Forecasting*, **11,** 273-287.

Brewster, K., 1996: Application of a Bratseth analysis scheme including Doppler radar data. *Preprints, 15th Conf. Wea. Anal. Forecasting*, Norfolk, VA, Amer. Meteor. Soc., 92-95.

Davies-Jones, R., R. J. Trapp, and H. B. Bluestein, 2001: Tornadoes and tornadic storms. Severe Convective Storms, I. *Charles A. Doswell, Ed., Amer. Meteor. Soc.***,** 167-221.

Gao, J., M. Xue, K. Brewster, F. Carr, and K. K. Droegemeier, 2002: New development of a 3DVAR system for a nonhydrostatic NWP model. *Preprint, 15th Conf. Num. Wea. Pred. and 19th Conf. Wea. Anal. Forecasting*, San Antonio, TX, Amer. Meteor. Soc., 339-341.

Gao, J.-D., M. Xue, A. Shapiro, and K. K. Droegemeier, 1999: A variational method for the analysis of three-dimensional wind fields from two Doppler radars. *Mon. Wea. Rev.*, **127,** 2128-2142.

Gao, J.-D., M. Xue, K. Brewster, and K. K. Droegemeier, 2004: A three-dimensional variational data analysis method with recursive filter for Doppler radars. *J. Atmos. Ocean. Tech.*, **21,** 457-469.

Harris, B. A. and G. Kelly, 2001: A satellite radiance-bias correction scheme for data assimilation. *Quart. J. Roy. Meteor. Soc.*, **127,** 1453-1468.

Hu, M., M. Xue, and K. Brewster, 2005: 3DVAR and Cloud analysis with WSR-88D Level-II Data for the Prediction of the Fort Worth Tornadic Thunderstorms. Part I: Cloud Analysis. *Mon. Wea. Rev., Submitted*.

Schaefer, J. T., 1990: The critical success index as an indicator of warning skill. *Wea.*

Forecasting, **5,** 570-575.

Smith, P. L., Jr., C. G. Myers, and H. D. Orville, 1975: Radar reflectivity factor calculations in numerical cloud models using bulk parameterization of precipitation processes. *J. Appl. Meteor.*, **14,** 1156-1165.

Tong, M. and M. Xue, 2005: Ensemble Kalman filter assimilation of Doppler radar data with a compressible nonhydrostatic model: OSSE Experiments. *Mon. Wea. Rev.*, submitted.

Xue, M., K. K. Droegemeier, V. Wong, A. Shapiro, and K. Brewster, 1995: *ARPS Version 4.0 User's Guide*. [Available at http://www.caps.ou.edu/ARPS], 380 pp.

Xue, M., K. K. Droegemeier, and V. Wong, 2000: The Advanced Regional Prediction System (ARPS) - A multiscale nonhydrostatic atmospheric simulation and prediction tool. Part I: Model dynamics and verification. *Meteor. Atmos. Physics*, **75,** 161-193.

Xue, M., K. K. Droegemeier, V. Wong, A. Shapiro, K. Brewster, F. Carr, D. Weber, Y. Liu, and D. Wang, 2001: The Advanced Regional Prediction System (ARPS) - A multi-scale nonhydrostatic atmospheric simulation and prediction tool. Part II: Model physics and applications. *Meteor. Atmos. Phys.*, **76,** 143-166.

Xue, M., D.-H. Wang, J.-D. Gao, K. Brewster, and K. K. Droegemeier, 2003: The Advanced Regional Prediction System (ARPS), storm-scale numerical weather prediction and data assimilation. *Meteor. Atmos. Physics*, **82,** 139-170.

Zhang, J., F. Carr, and K. Brewster, 1998: ADAS cloud analysis. *Preprints, 12th Conf. on Num. Wea. Pred.*, Phoenix, AZ., Amer. Met. Soc., 185-188.

Zhang, J., 1999: Moisture and Diabatic Initialization Based on Radar and Satellite Observation, Ph.D., School of Meteorology, University of Oklahoma, 194pp.

List of Tables

Table 1. List of 3-km experiments and their main characteristics.

Table 1. List of 3-km experiments and their main characteristics.

Experiment	Use of Reflectivity	Use of Radial velocity	Mass divergence constraint	
			Dimension	Weighting Coefficients
CNTLVR	Yes	Yes	2D	$\alpha\lambda_c = 1000$, $\beta=0$
CNTLZ	Yes	No	N.A.	$\lambda_c=0$
VR	No	Yes	2D	$\alpha\lambda_c = 1000$, $\beta=0$
NoDiv	Yes	Yes	N.A.	$\lambda_c=0$
Div2Da	Yes	Yes	2D	$\alpha\lambda_c = 500$, $\beta=0$
Div2Db	Yes	Yes	2D	$\alpha\lambda_c = 2000$, $\beta=0$
Div3Da	Yes	Yes	3D	$\alpha\lambda_c = 1000$, $\beta\lambda_c = 100$
Div3Db	Yes	Yes	3D	$\alpha\lambda_c = \beta\lambda_c = 1000$

List of Figures

Fig. 5. Similar to Fig. 3, except that they are predicted wind and vorticity fields from experiment CNTLZ at 15 minute intervals from 0015 UTC through 0045 UTC 29 March, 2000.

Fig. 6. Equitable threat scores of predicted reflectivity for the 5 dBZ (a), 15 dBZ (b), 30 dZB (c), and 45 dBZ (d) threshold values from experiments CNTLVR, CNTLZ and NoDiv.

Fig. 7. Similar to Fig. 2, except that it is predicted reflectivity field from experiment VR at 0030 UTC 29 March, 2000.

Fig. 8 The vertical velocity fields at 5 km MSL (left column) and cross section of vertical velocity along the line in figure (a) (right column) from the assimilation output of experiments CNTLVR, CNTLZ, and VR

Fig. 9. Similar to Fig. 2, except that they are predicted reflectivity fields from experiments CNTLVR (a), NoDiv (b), Div2Da (c), Div2Db (d), Div3Da (e), and Div3Db (f), at 0030 UTC 29 March, 2000.

Fig. 10. Similar to Fig. 3, except that they are predicted wind and vorticity fields from experiments NoDiv, Div2Da, Div2Db, Div3Da, and Div3Db, at 0030 UTC 29 March, 2000.

Fig. 11. Same as Fig. 6 but for experiments CNTLVR, Div2Da, and Div2Db.

Fig. 12. Same as Fig. 6 but for experiments CNTLVR, Div3Da, Div3Db, and NoDiv.

Fig. 13 The vertical velocity fields at 5 km MSL from the assimilation output of experiments CNTLVR, NoDiv, Div2Da, Div2Db, Div3Da, and Div3Db.
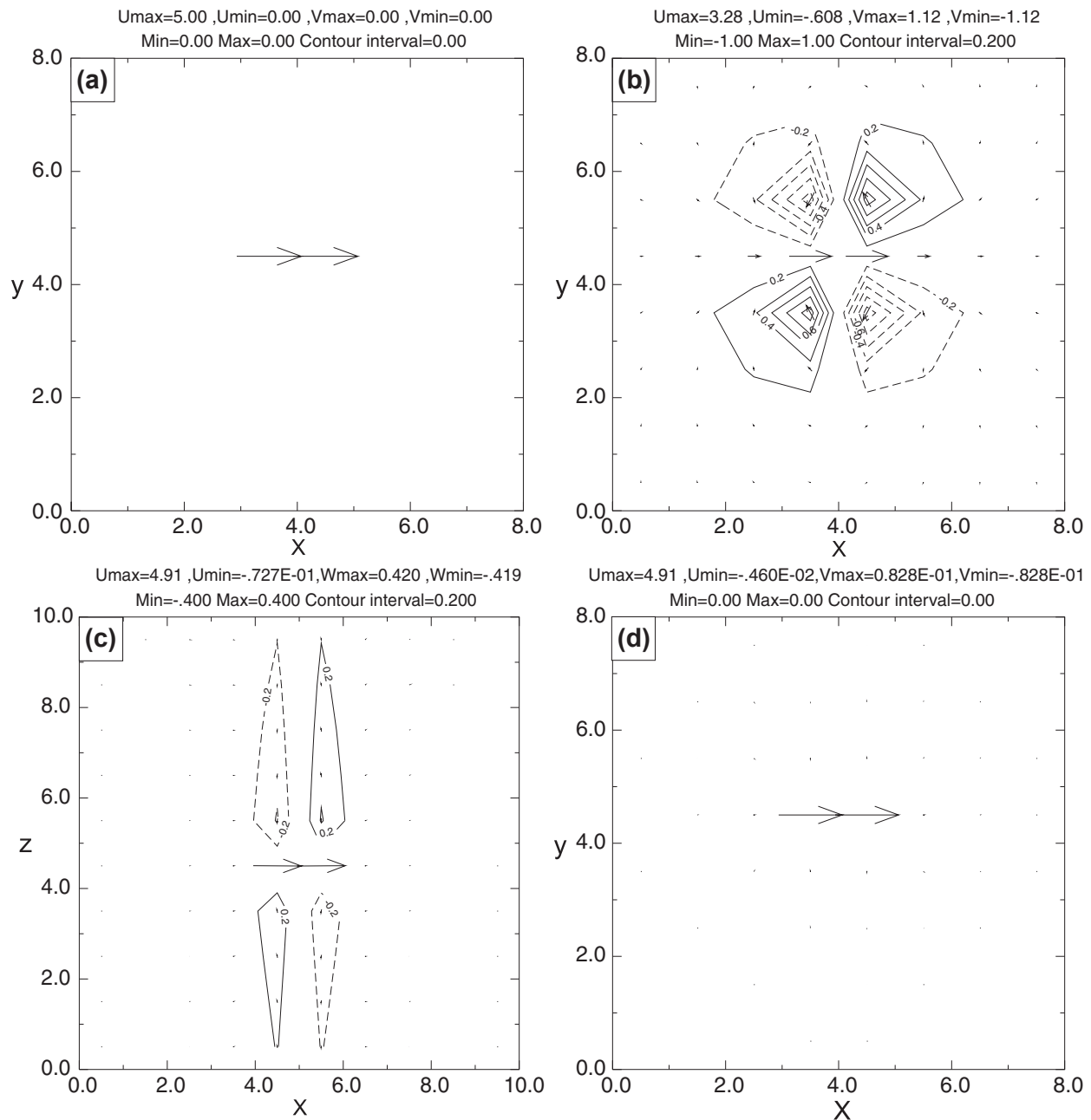
Umax=5.00 ,Umin=0.00 ,Vmax=0.00 ,Vmin=0.00
Min=0.00 Max=0.00 Contour interval=0.00

Umax=3.28 ,Umin=-.608 ,Vmax=1.12 ,Vmin=-1.12
Min=-1.00 Max=1.00 Contour interval=0.200

Umax=4.91 ,Umin=-.727E-01,Wmax=0.420 ,Wmin=-.419
Min=-.400 Max=0.400 Contour interval=0.200

Umax=4.91 ,Umin=-.460E-02,Vmax=0.828E-01,Vmin=-.828E-01
Min=0.00 Max=0.00 Contour interval=0.00

Fig. 1. Results of 3DVAR analyzing a single radial wind measurement (pointing in positive *x* direction) with different mass divergence constraints. The background wind is zero. a) wind analysis without applying mass divergence constraint, b) the x-y cross-section of u-v wind analyzed with a 2D (horizontal) mass divergence constraint, c) x-z cross-section of u-w wind after applying a 3D mass divergence constraint, and d) as b) but with a 3D mass divergence constraint. The wind units are m s^{-1}.
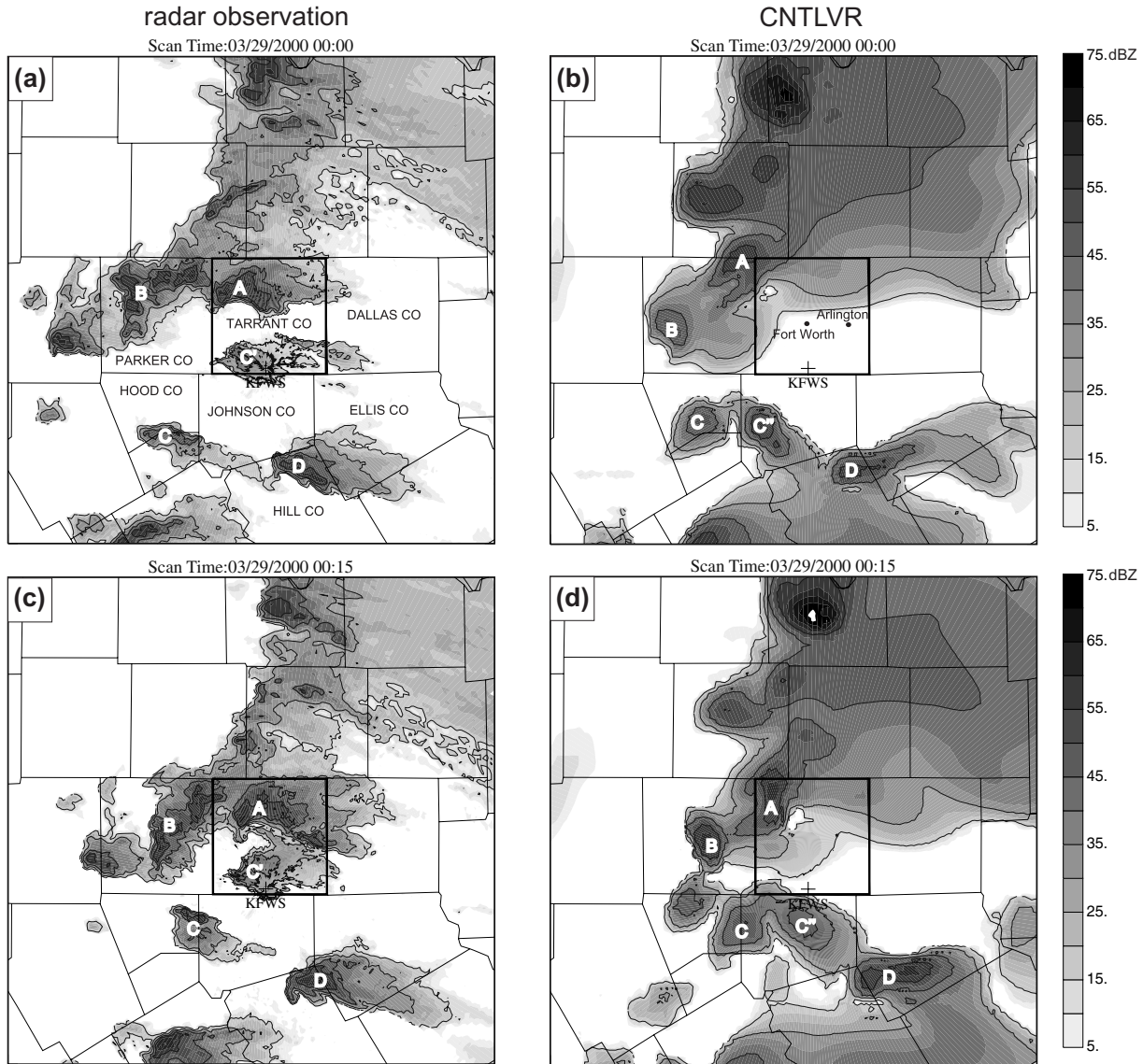
Fig. 2. Observed reflectivity fields at 1.45° elevation of the Fort Worth radar (marked as KFWS) based on Level-II data (left column), and predicted reflectivity at the same elevation from the control experiment CNTLVR (right column), at 15 minute intervals from 0000 UTC to 0100 UTC 29 March, 2000. Major storm cells are marked by capital letters. Fort Worth and Arlington are marked as dot in (b). Tarrant County is highlighted and about 50×50 km^2 in size. The domain shown is about 200 km on each side, representing the portion of 3-km grid between 100 and 300 km in east-west direction and from 60 to 260 km in north-south direction. The reflectivity contours are at 15, 30, 45 and 55 dBZ and the shaded contour interval is 5 dBZ. Counties around Fort Worth are marked in (a).
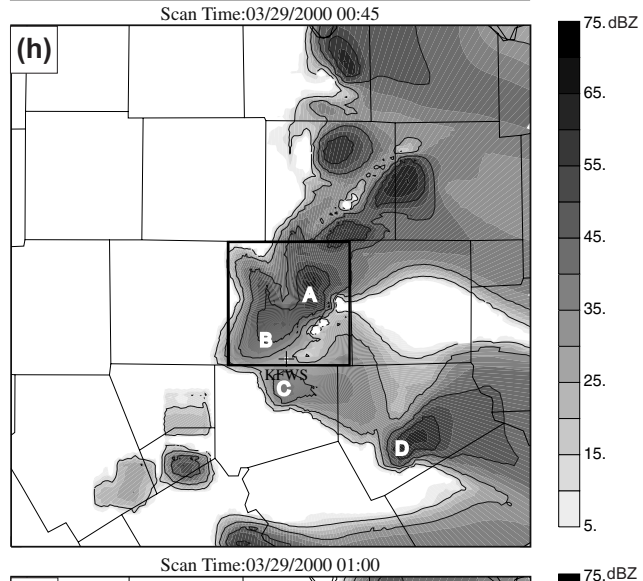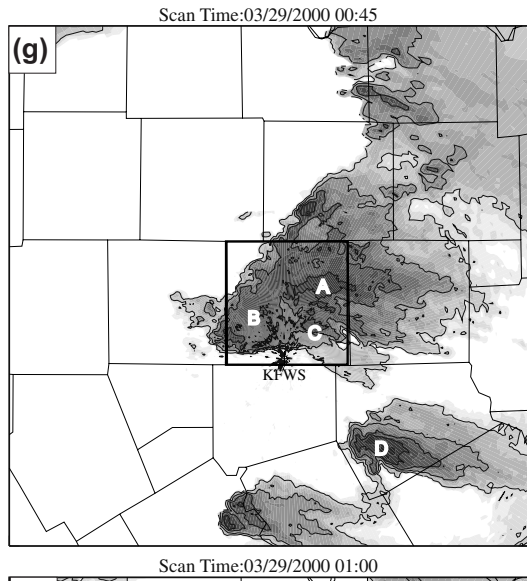
radar observation

CNTLVR

Scan Time:03/29/2000 00:30

Scan Time:03/29/2000 00:30

(e)

(f)

Scan Time:03/29/2000 00:45

Scan Time:03/29/2000 00:45

(g)

(h)

Scan Time:03/29/2000 01:00

Scan Time:03/29/2000 01:00
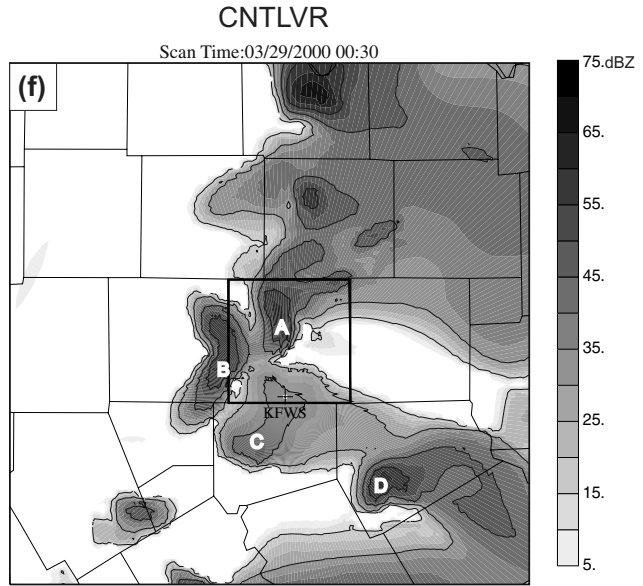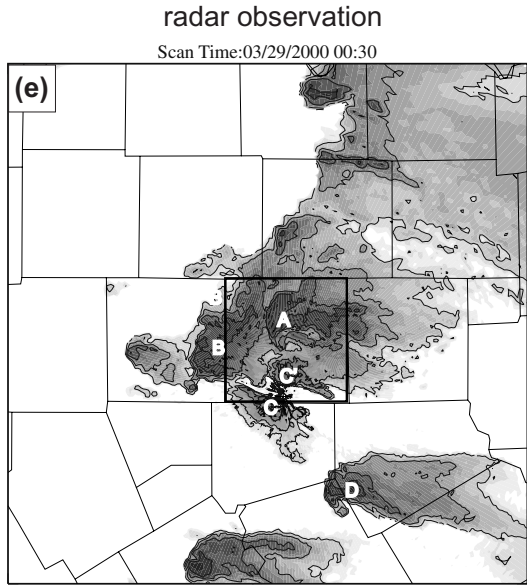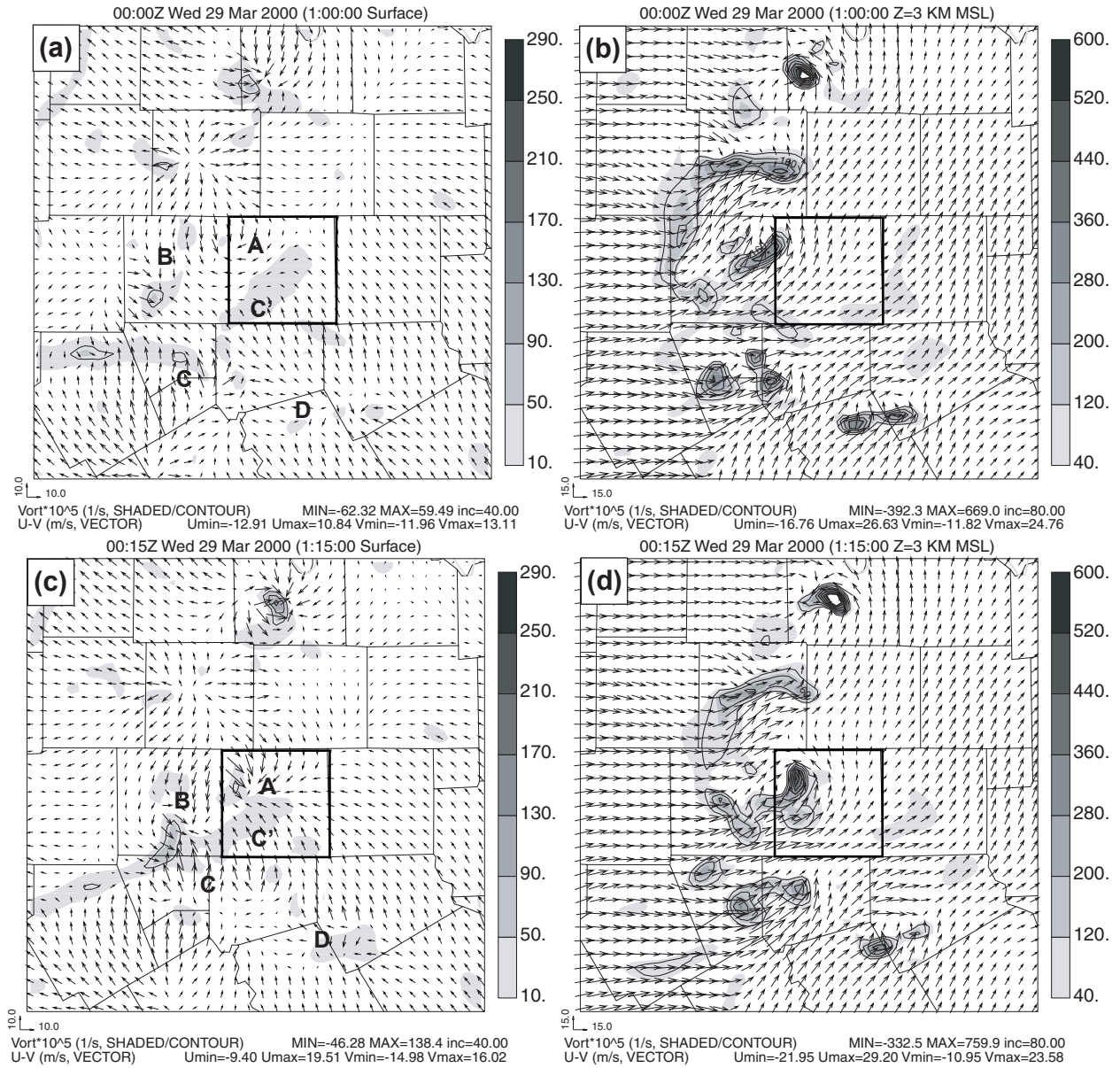
(i)

(j)

Fig. 2. Continued.

35
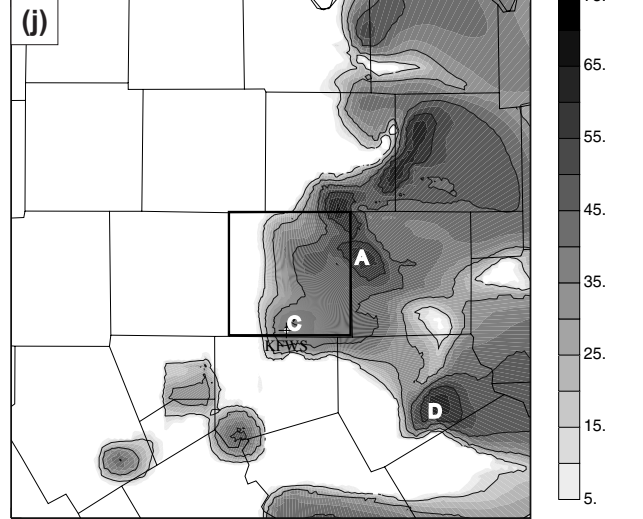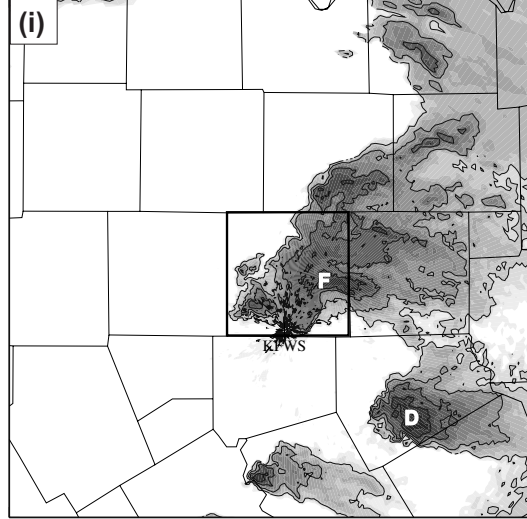
Fig. 3. Predicted wind and vertical vorticity fields at the surface (left column) and 3 km MSL (right column) from control experiment CNTLVR corresponding to the times of Fig. 2. The domains shown are the same as in Fig. 2. The capital letters in the left column are the positions of the observed storms.
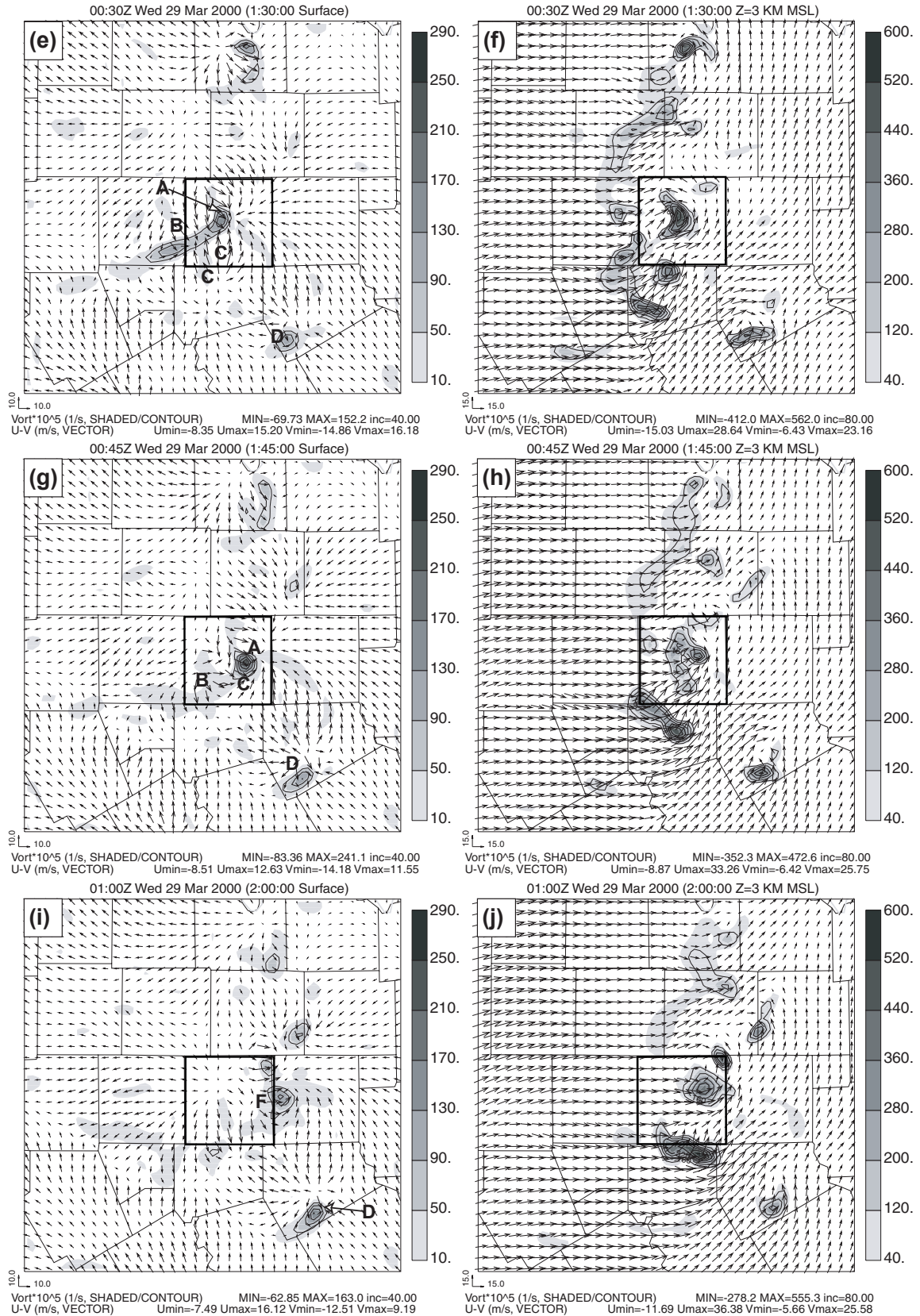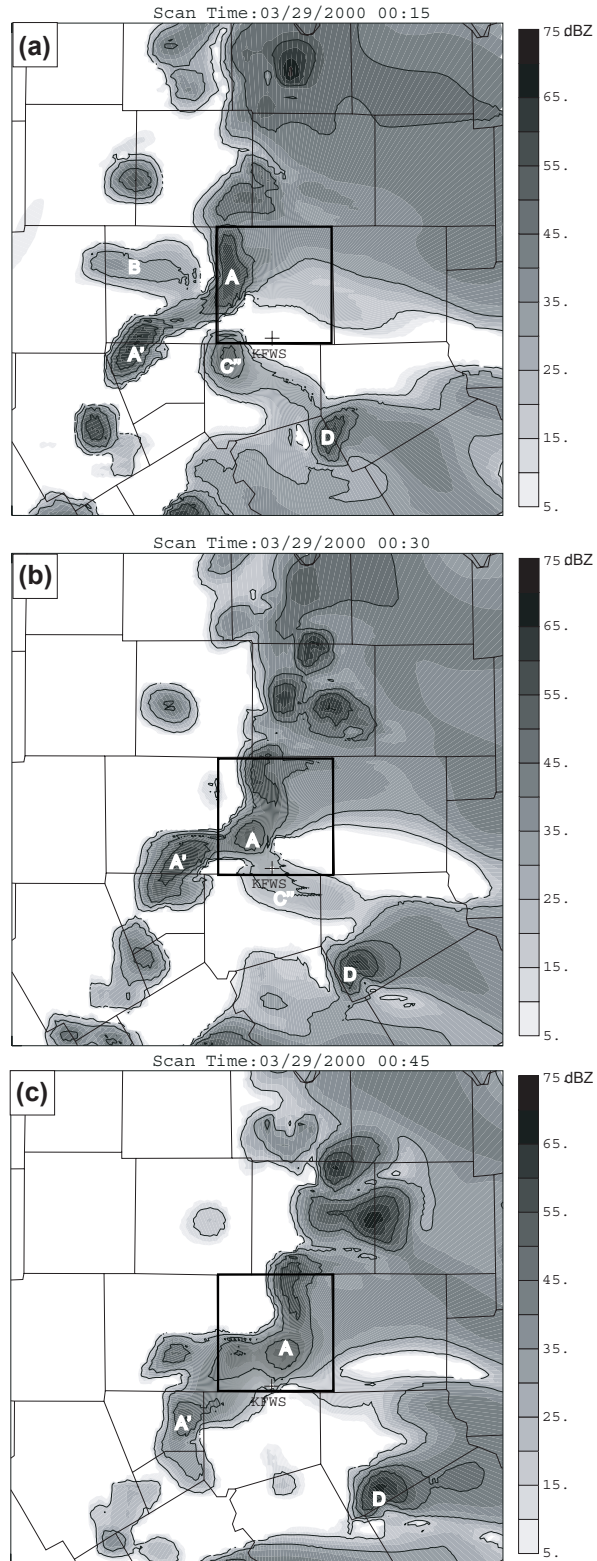
Fig. 3. Continued.

Fig. 4. Similar to right column of Fig. 2, except that they are predicted reflectivity from experiment CNTLZ at 15 minute intervals from 0015 UTC through 0045 UTC 29 March, 2000.
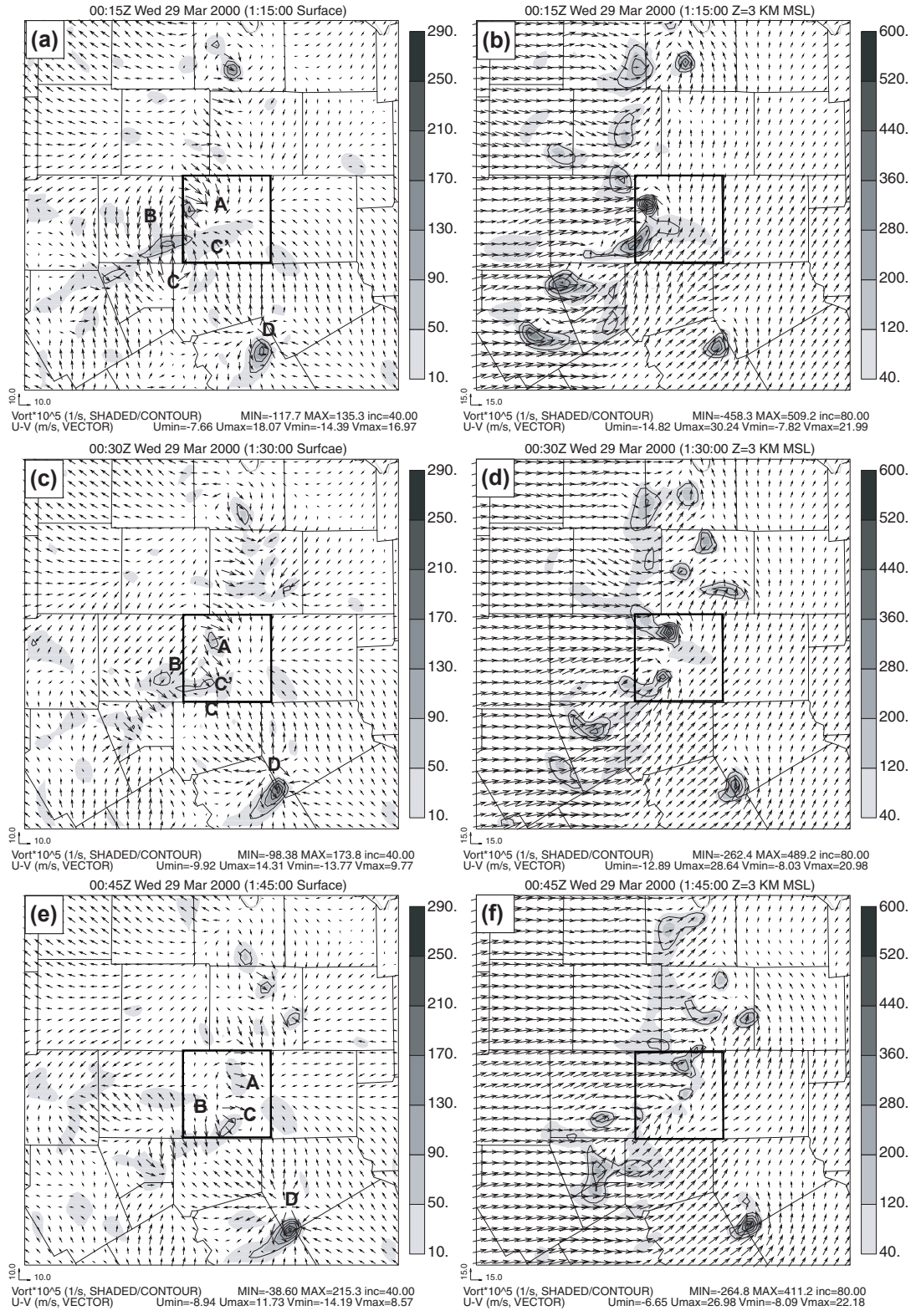
Fig. 5. Similar to Fig. 3, except that they are predicted wind and vorticity fields from experiment CNTLZ at 15 minute intervals from 0015 UTC through 0045 UTC 29 March, 2000.
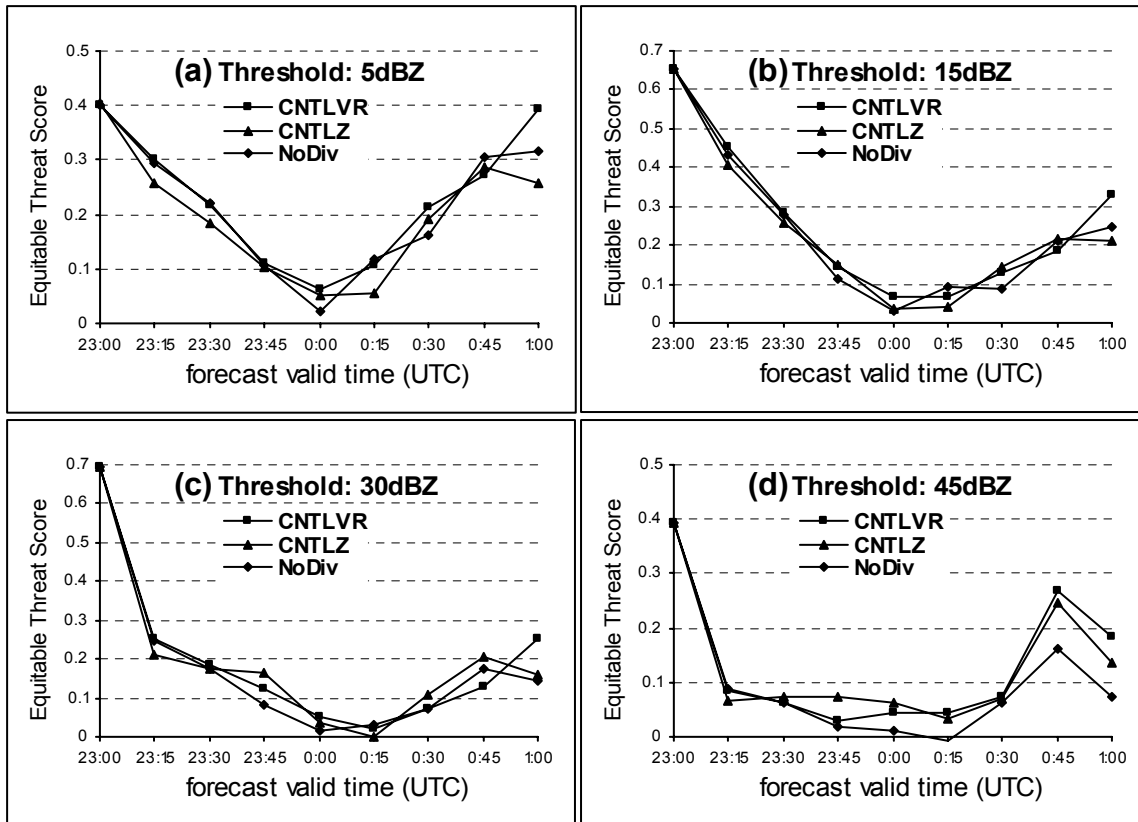
Fig. 6. Equitable threat scores of predicted reflectivity for the 5 dBZ (a), 15 dBZ (b), 30 dZB (c), and 45 dBZ (d) threshold values from experiments CNTLVR, CNTLZ and NoDiv.
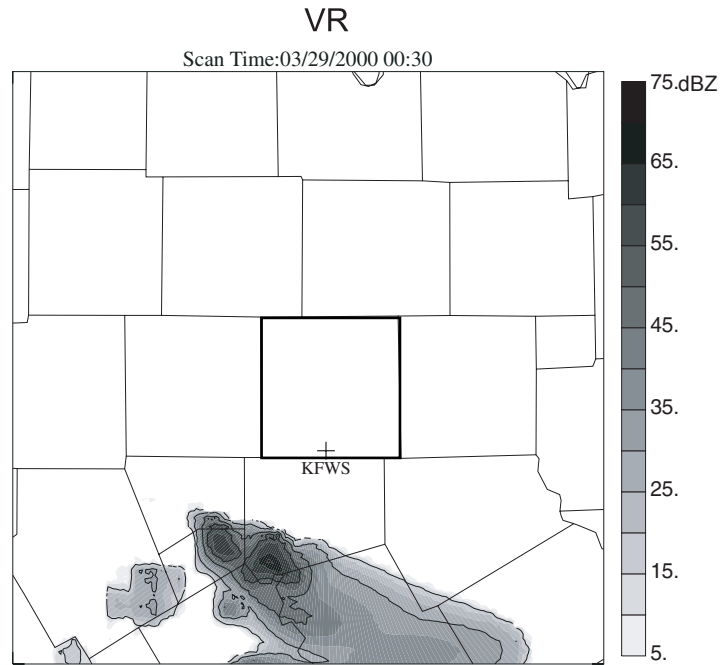
Fig. 7. Similar to Fig. 2, except that it is predicted reflectivity field from experiment VR at 0030 UTC 29 March, 2000.

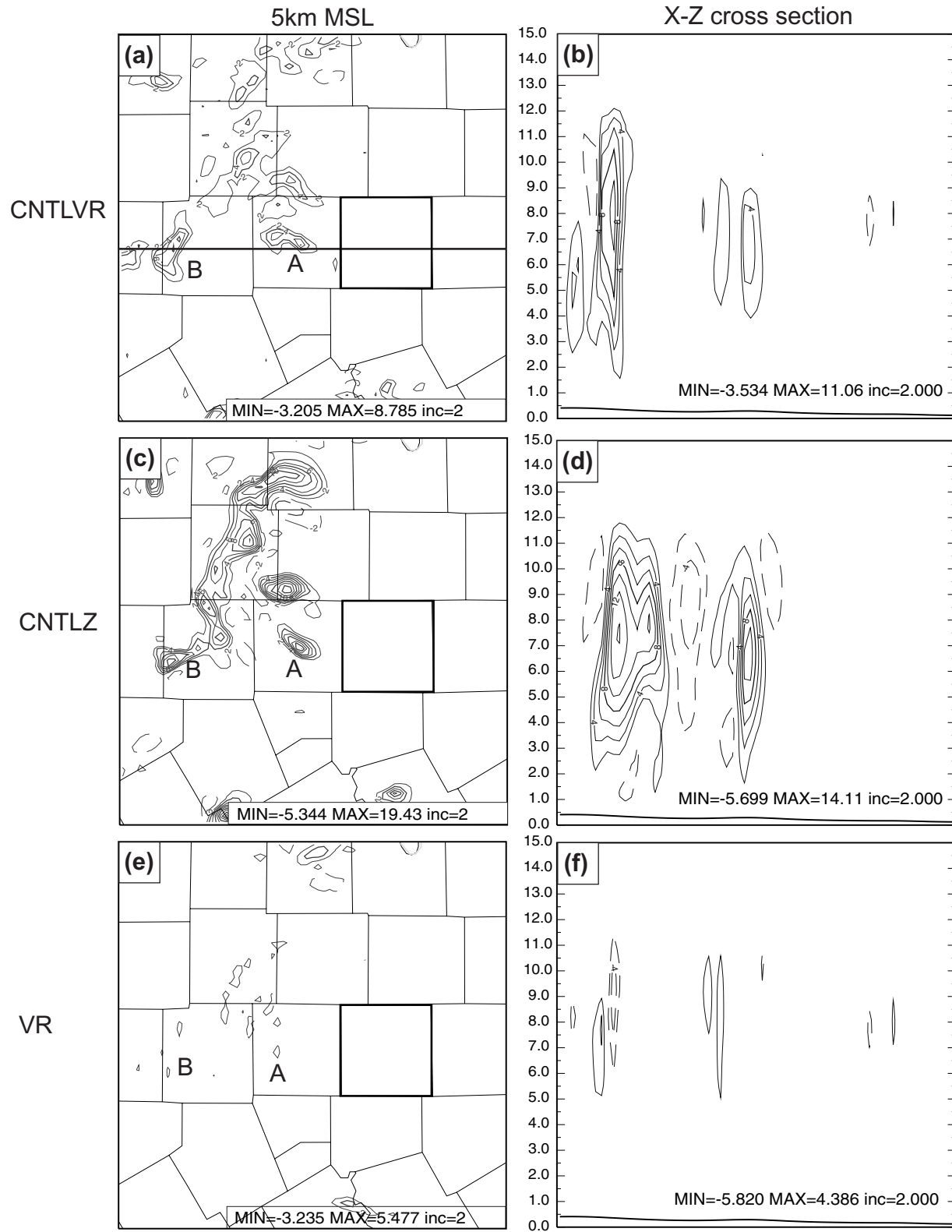Fig. 8 The vertical velocity fields at 5 km MSL (left column) and cross section of vertical velocity along the line in figure (a) (right column) from the assimilation output of experiments CNTLVR, CNTLZ, and VR.
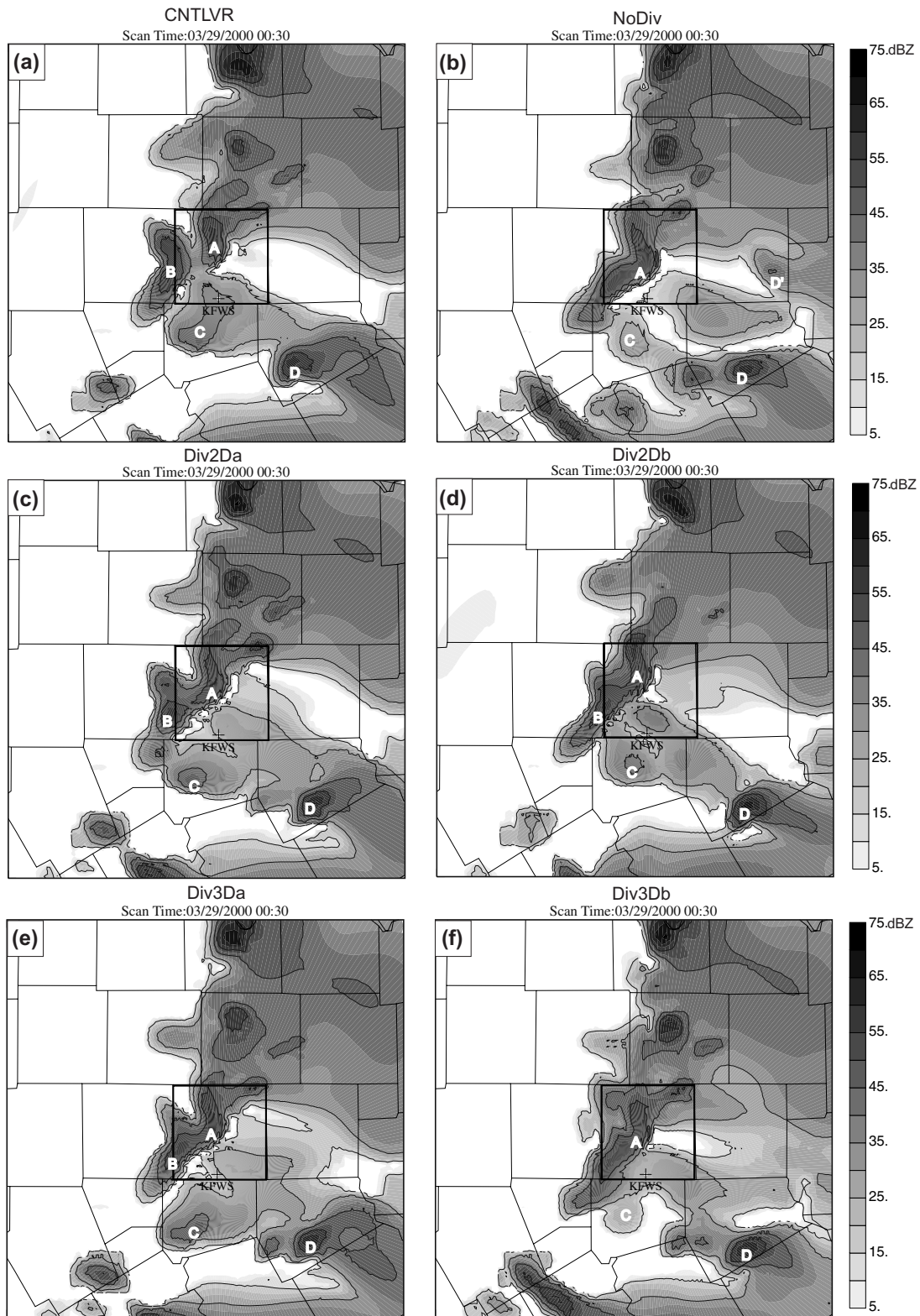
Fig. 9. Similar to Fig. 2, except that they are predicted reflectivity fields from experiments CNTLVR (a), NoDiv (b), Div2Da (c), Div2Db (d), Div3Da (e), and Div3Db (f), at 0030 UTC 29 March, 2000.
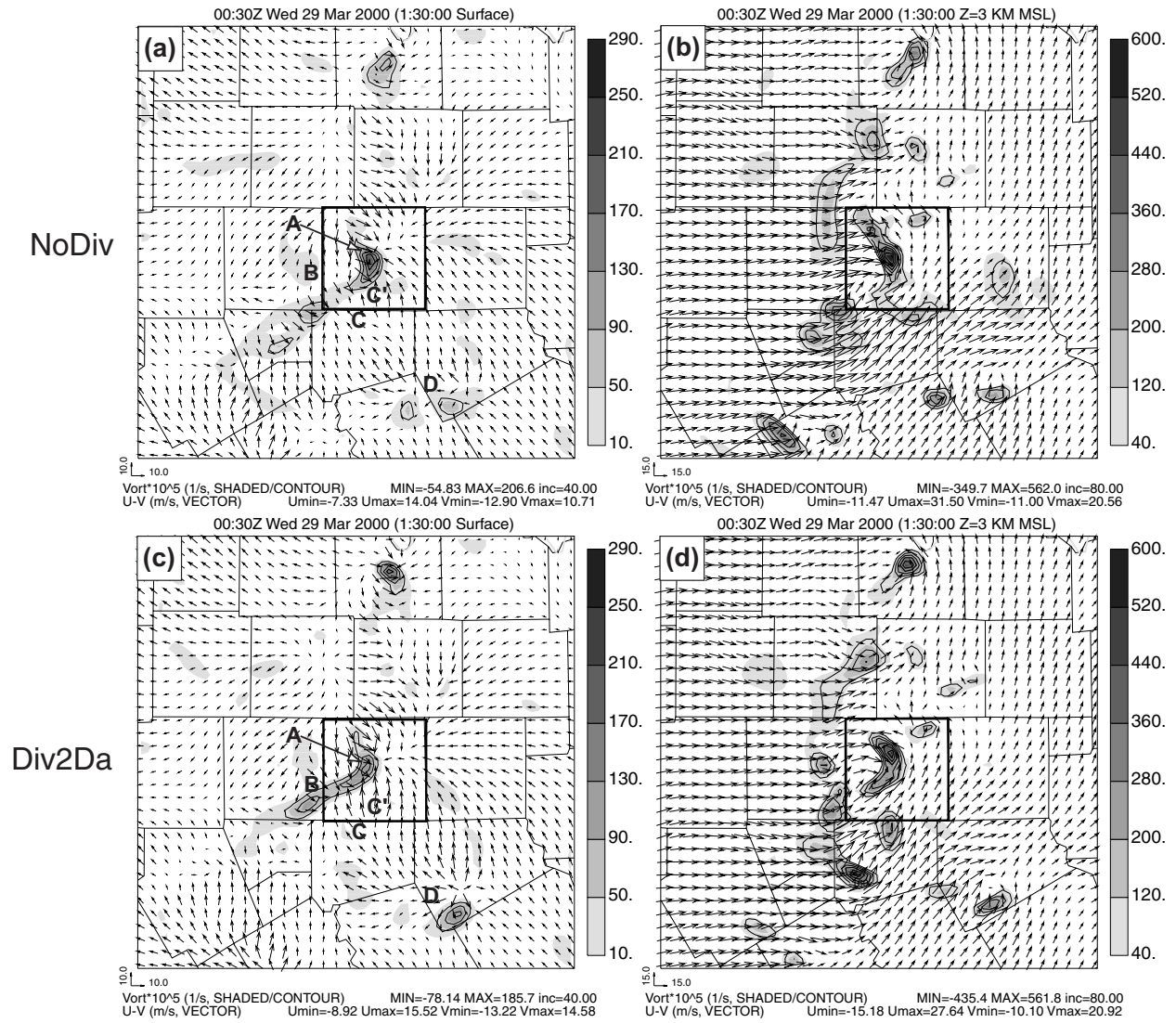
Fig. 10. Similar to Fig. 3, except that they are predicted wind and vorticity fields from experiments NoDiv, Div2Da, Div2Db, Div3Da, and Div3Db, at 0030 UTC 29 March, 2000.

Div2Db

00:30Z Wed 29 Mar 2000 (1:30:00 Surface)

(e)

A
B
C'
C

D

Vort*10^5 (1/s, SHADED/CONTOUR)   MIN=-47.65 MAX=207.7 inc=40.00
U-V (m/s, VECTOR)   Umin=-8.86 Umax=17.40 Vmin=-15.27 Vmax=12.72

00:30Z Wed 29 Mar 2000 (1:30:00 Z=3 KM MSL)

(f)

Vort*10^5 (1/s, SHADED/CONTOUR)   MIN=-274.0 MAX=496.8 inc=80.00
U-V (m/s, VECTOR)   Umin=-18.66 Umax=26.72 Vmin=-9.05 Vmax=21.84

Div3Da

00:30Z Wed 29 Mar 2000 (1:30:00 Surface)

(g)

A
B
C'
C

D

Vort*10^5 (1/s, SHADED/CONTOUR)   MIN=-70.41 MAX=154.0 inc=40.00
U-V (m/s, VECTOR)   Umin=-8.60 Umax=14.86 Vmin=-15.04 Vmax=13.57

00:30Z Wed 29 Mar 2000 (1:30:00 Z=3 KM MSL)

(h)

Vort*10^5 (1/s, SHADED/CONTOUR)   MIN=-399.3 MAX=468.8 inc=80.00
U-V (m/s, VECTOR)   Umin=-12.69 Umax=28.71 Vmin=-10.39 Vmax=19.91

Div3Db

00:30Z Wed 29 Mar 2000 (1:30:00 Surface)

(i)

A
B
C'
C

D

Vort*10^5 (1/s, SHADED/CONTOUR)   MIN=-54.75 MAX=187.0 inc=40.00
U-V (m/s, VECTOR)   Umin=-9.41 Umax=12.29 Vmin=-13.28 Vmax=12.03

00:30Z Wed 29 Mar 2000 (1:30:00 Z=3 KM MSL)

(j)

Vort*10^5 (1/s, SHADED/CONTOUR)   MIN=-376.4 MAX=529.4 inc=80.00
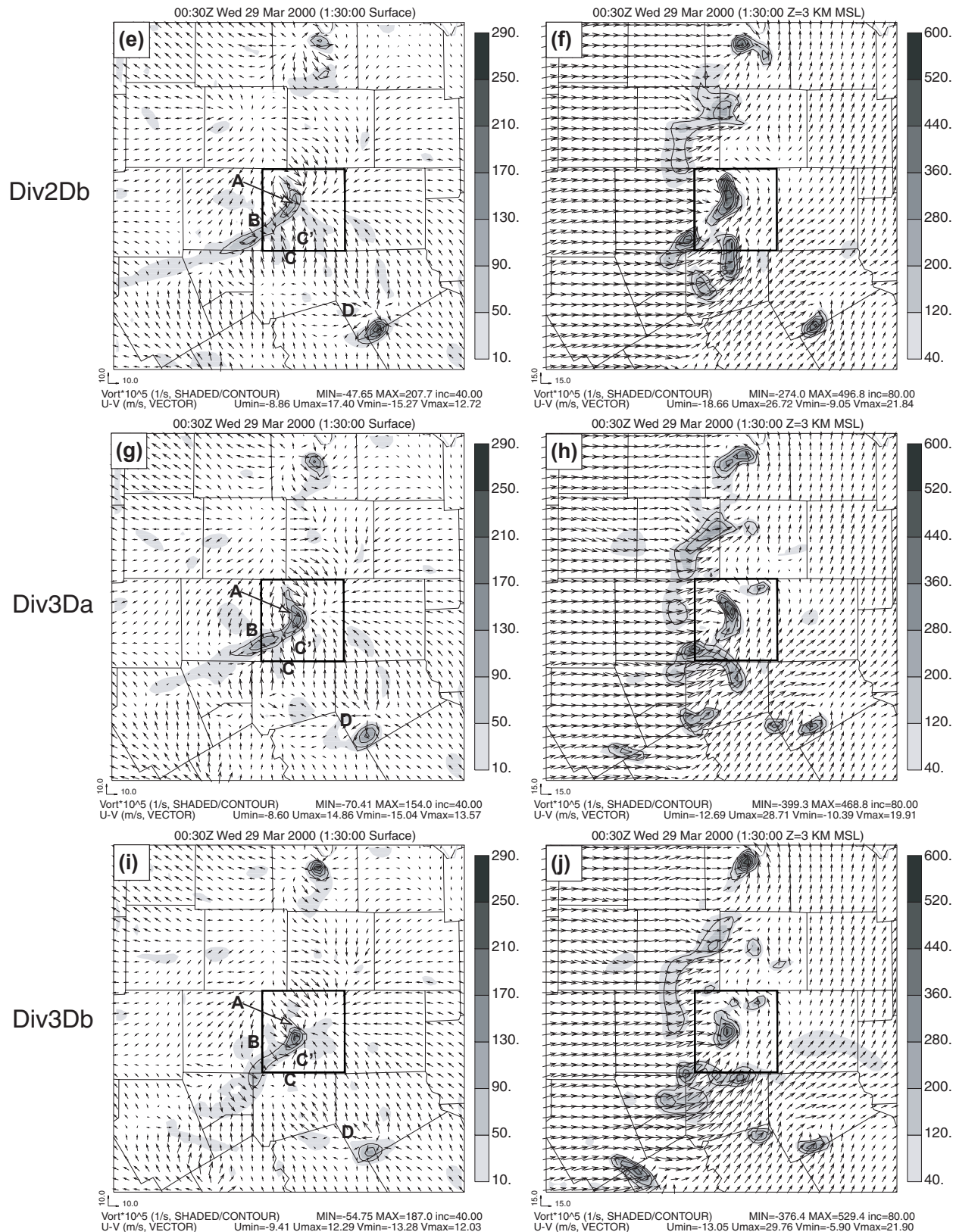U-V (m/s, VECTOR)   Umin=-13.05 Umax=29.76 Vmin=-5.90 Vmax=21.90
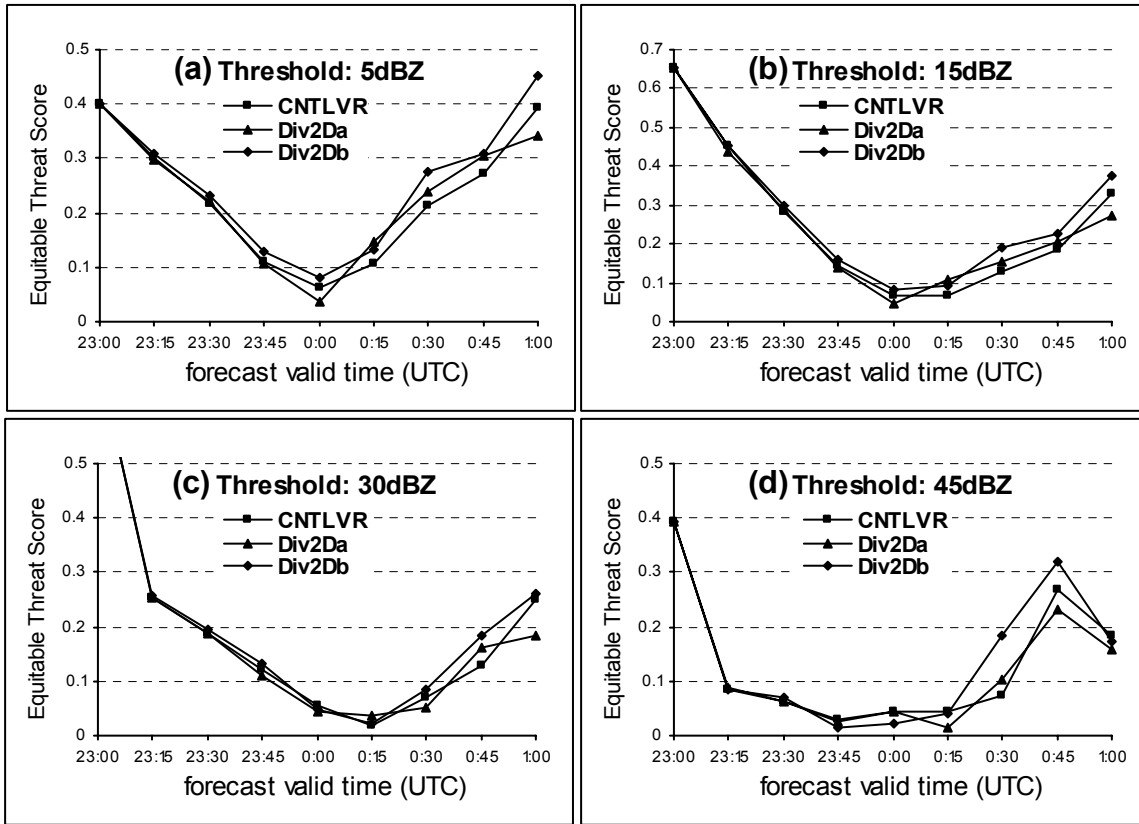
Fig. 10. Continued.

Fig. 11. Same as Fig. 6 but for experiments CNTLVR, Div2Da, and Div2Db.

Fig. 12. Same as Fig. 6 but for experiments CNTLVR, Div3Da, Div3Db, and NoDiv.

CNTLVR

(a)

B   A

MIN=-3.205 MAX=8.785 inc=2.000

NoDiv

(b)

B   A

MIN=-5.213 MAX=14.73 inc=2.000

Div2Da

(c)

B   A

MIN=-4.613 MAX=11.67 inc=2.000

Div2Db

(d)

B   A

MIN=-1.979 MAX=5.715 inc=2.000

Div3Da

(e)

B   A

MIN=-3.562 MAX=10.13 inc=2.000

DIv3Db
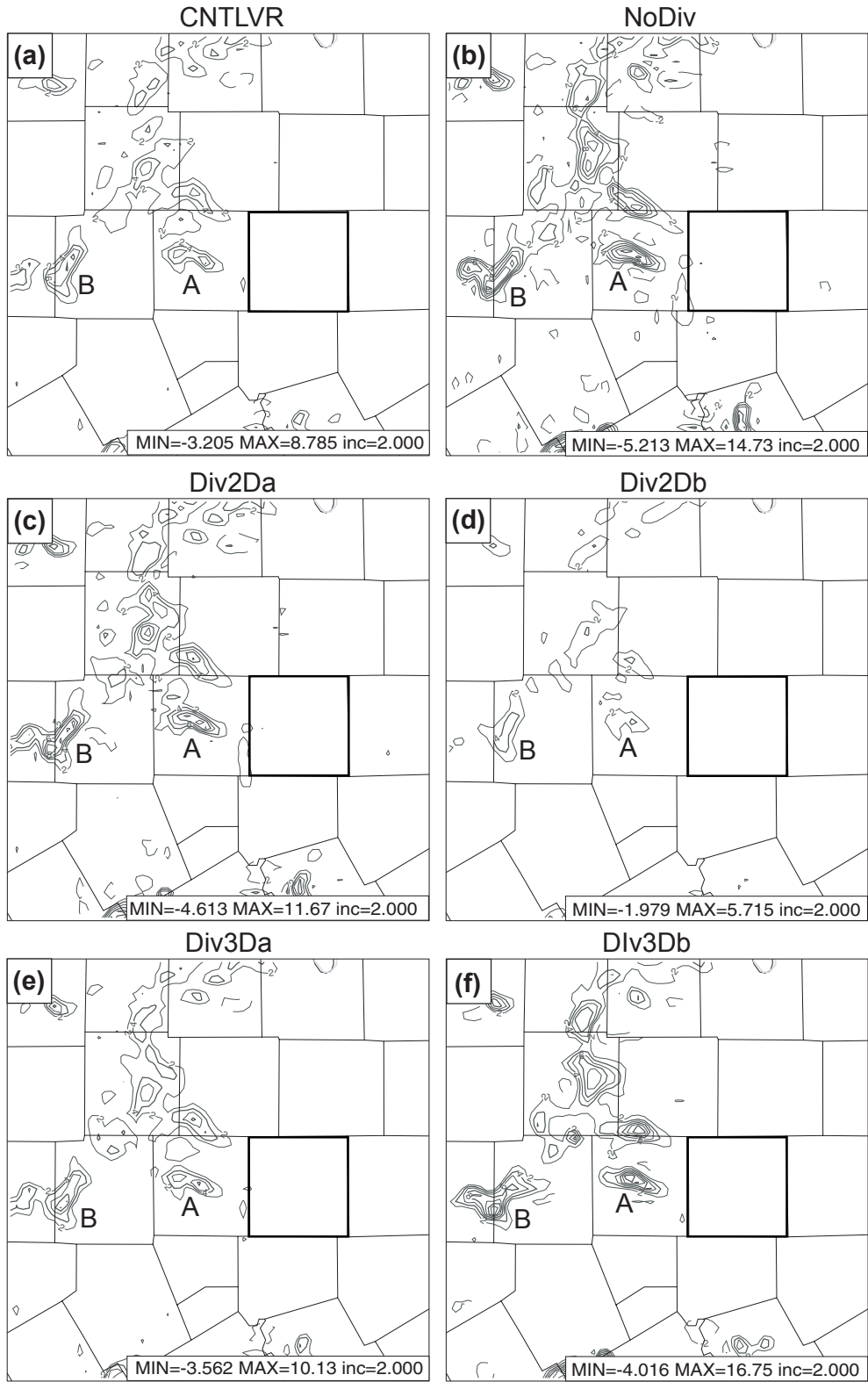
(f)

B   A

MIN=-4.016 MAX=16.75 inc=2.000

Fig. 13 The vertical velocity fields at 5 km MSL from the assimilation output of experiments CNTLVR, NoDiv, Div2Da, Div2Db, Div3Da, and Div3Db.